Check for updates

Advanced Materials

ADVANCED MATERIALS
www.advmat.de

RESEARCH ARTICLE

Targeting Endoplasmic Reticulum Stress-ROS-Inflammation Cycle With Antibacterial Heterojunctions for Periodontitis Therapy

Wanxi Chen[1,2] | Wenxuan He[1] | Wenyu Dai[2] | Bin Li[2] | Fan Yang[2,3] | Tian Chen[2] | Rui Shu[2] | Ding Bai[2] | Yi Deng[1,4] | Hui Xu[1,2]

[1]West China Hospital of Stomatology, School of Chemical Engineering, Sichuan University, Chengdu, China | [2]State Key Laboratory of Oral Diseases, National Clinical Research Center for Oral Diseases, Department of Orthodontics and Pediatric Dentistry, West China Hospital of Stomatology, Sichuan University, Chengdu, China | [3]Hospital of Stomatology, Guangdong Provincial Key Laboratory of Stomatology, Guanghua School of Stomatology, Sun Yat-Sen University, Guangzhou, China | [4]State Key Laboratory of Advanced Polymer Materials, Sichuan University, Chengdu, China

Correspondence: Yi Deng (dengyibandeng@scu.edu.cn) | Hui Xu (xhhx@scu.edu.cn)

Received: 30 June 2026 | **Revised:** 25 September 2026 | **Accepted:** 9 October 2026

Keywords: antibacterial | bacterial infection | heterojunction | osteogenesis | periodontitis

ABSTRACT

In periodontitis, recalcitrant biofilms and the vicious endoplasmic reticulum (ER) stress-ROS-inflammation cycle cause persistent inflammatory osteolysis. However, current treatments mainly alleviate infection and inflammation, without targeting this ER stress-centered etiological circuit. Herein, we report the de novo design of an ER-regulating heterojunction (ERR-HJ), composed of cobalt selenide (CoSe), Ti_3C_2 MXene, and taurine, for periodontitis treatment via bacterial clearance, ER homeostasis maintenance, and alveolar bone regeneration. Our studies demonstrate that the unique structure of the CoSe/Ti_3C_2 heterojunction can scavenge ROS and easily transfer electrons from H_2O_2 to bacterial membranes, which disrupts bacterial respiration and metabolism. At the cellular level, the heterojunction with taurine activates selenoprotein metabolism, restores redox balance, and alleviates ER stress by dampening the PERK-CHOP pathway, collectively reprogramming macrophages towards a tissue-regenerative M2 phenotype while inhibiting their osteoclastogenic differentiation. Strikingly, the osteogenic differentiation of human periodontal ligament cells is profoundly boosted. In periodontitis models, the ERR-HJ promotes tissue repair and reduces alveolar bone resorption through concomitant suppression of oxidative stress, ER stress, and inflammation, suggesting the disruption of the self-perpetuating cycle. This work furnishes an intriguing avenue for developing innovative heterojunction biomaterials to treat bacterial infection-associated disorders by integrating bacterial killing and ER stress-ROS-inflammation cycle inhibition.

1 | Introduction

Periodontitis, a prevalent biofilm-driven chronic inflammatory disorder, affects approximately one billion individuals worldwide and has shown a continuous increase over the past decades [1–3]. This disease evokes persistent immune activation and progressive destruction of alveolar bone. The pathological features not only compromise masticatory function and facial esthetics, often culminating in tooth loss and profoundly impairing quality of life, but are also considered a risk factor for the progression of

Wanxi Chen and Wenxuan He contributed equally to this work.

All rights reserved, including rights for text and data mining and training of artificial intelligence technologies or similar technologies.
© 2026 Wiley-VCH GmbH

systemic diseases such as diabetes and cardiovascular disease, underscoring its significant clinical relevance [4]. Current clinical interventions, including mechanical debridement, antibiotic administration, and surgical approaches, show effectiveness in temporary resolution of inflammation, yet largely fall short in achieving sustained clinical remission [5, 6]. This limitation stems from the failure to resolve the disease's underlying etiology.

Endoplasmic reticulum (ER) stress is a major intracellular stress arising from the accumulation of misfolded proteins and activation of the unfolded protein response (UPR), acting as a critical etiological factor in periodontitis [7–9]. Studies on clinical samples have shown that ER stress is activated in human periodontitis tissues, a stark contrast to its inactive "off" state in healthy periodontal tissue [10]. Upon the accumulation of bacterial biofilms on dental surfaces, macrophages infiltrate and phagocytose the invading bacteria and are concomitantly exposed to virulence factors (e.g., lipopolysaccharides, LPS, and pore-forming toxins) that elicit ER stress by disrupting Ca^{2+} balance and engaging TLR4-GRP94 signaling pathways [11, 12]. This process prompts macrophages to release large amounts of pro-inflammatory cytokines and generate massive reactive oxygen species (ROS) [13]. In turn, ROS exacerbates protein misfolding and UPR activation, thereby forming a vicious amplification loop of oxidative stress-ER stress [7]. This loop potently upregulates osteoclastogenic transcriptional programs to dramatically boost osteoclast differentiation of macrophages, ultimately leading to bone resorption [14]. It is noteworthy that even after bacterial clearance, the established ER stress state persists as a dysregulated host response that impairs tissue repair [15]. Therefore, in periodontitis niches, the two intertwined pathogenic factors, bacterial infection and macrophage-derived ER stress elevation, create a self-perpetuating vicious cycle of intracellular stress generation, inflammation, and tissue breakdown. This understanding highlights the pivotal need to develop an innovative therapeutic tactic that can simultaneously eradicate the two fundamental aspects of periodontitis pathogenesis.

Heterojunction materials, which are constructed by contact coupling of two or more semiconductors with dissimilar electron affinities and unequal bandgaps, have emerged as a promising platform to concurrently address bacterial infection and intracellular stress owing to their intrinsic catalytic behavior and variable chemical composition of semiconductors that can be tailored through rational molecular design [16–18]. By matching energy band structure and accelerating interfacial electron/hole transfer, heterojunctions under external activation can effectively catalyze oxygen, water, and hydrogen peroxide from pathological microenvironments to generate a high yield of ROS [19–22]. These broad-spectrum bactericidal ROS dramatically destroy bacterial membranes and disorganize intracellular organelle-like structures, thereby achieving rapid disinfection [18, 19]. Recent advances have directed bacterium–material electron transfer to disrupt bacterial metabolic homeostasis, thus potentiating antimicrobial effects [23, 24]. Critically, these effects were achieved without concomitant ROS scavenging, or even accompanied by elevated ROS production. This detrimental trade-off—the very ROS surge that mediates pathogen clearance—simultaneously drives oxidative tissue damage and undermines long-term tissue repair. These limitations underscore the need for a new strategy that retains bactericidal potency while mitigating oxidative damage. The compositional tunability of heterojunctions allows for the incorporation of antioxidative elements (Ce, Cu, Zn, Mn, Se, etc.) to modulate intracellular stress responses, such as oxidative stress [19, 25, 26]. Among these antioxidative elements, selenium (Se) is an indispensable constituent of selenoproteins in the ER and has been shown to maintain ER homeostasis through promoting proper protein folding and facilitating the degradation of misfolded proteins [27–29]. Therefore, we hypothesize that a Se-incorporated heterojunction may be a prospective material that can collectively address the pathogenic factors of bacterial infection and ER stress. However, the clinical adoption of Se-incorporated heterojunctions still faces three critical challenges, especially in periodontitis therapy: first, ROS-dependent disinfection inevitably exacerbates oxidative injury and inflammation in host tissue [30]; second, the direct introduction of heterojunctions into the body primarily elicits macrophage activation and subsequent foreign body response [31]; third, the underlying mechanism of their ER stress-alleviating properties largely remains elusive.

To address these constraints, here we de novo develop an ER-regulating heterojunction (ERR-HJ) composed of cobalt selenide (CoSe), Ti_3C_2 MXene, and taurine. The material design in this study originates from three key considerations: (1) Redox-active Co ions with plenty of unfilled d orbitals can serve as active sites to catalyze and deplete ROS by optimizing the binding to oxygen species [32]; (2) Ti_3C_2 MXene, an emerging 2D material, is a biocompatible semiconductor with excellent near-infrared (NIR) light absorption capability [33, 34]; (3) Taurine, a sulfur-containing amino acid, has been reported to possess ER stress-alleviating properties [35, 36]; in addition, the taurine coating reduces direct contact between the heterojunction and the host. In infection, different from the conventional ROS generation-driven antibacterial modality, ERR-HJ absorbs H_2O_2-derived electrons and facilitates their transfer to bacterial membranes in H_2O_2-rich biofilm infection environments, perturbing the bacterial respiratory chain and energy metabolism, contributing to bacterial clearance. For healing promotion, ERR-HJ exhibits prominent multienzyme-mimetic activities to scavenge ROS and alleviate oxidative injury. By reprogramming macrophages toward a pro-regenerative M2 phenotype, it attenuates inflammatory responses and helps reestablish osteoimmune balance, which enhances osteogenic differentiation of periodontal ligament cells and suppresses receptor activator of nuclear factor κB ligand (RANKL)-driven osteoclastogenesis. Mechanistic insights from transcriptomic analysis reveal that the activation of seleno-amino acid synthesis and selenoprotein metabolism significantly restores ER-redox balance and suppresses the ER-associated PERK-CHOP pathway. In vivo studies employing rat periodontitis models corroborate that ERR-HJ can mitigate alveolar bone loss and promote periodontal tissue regeneration through disrupting the ER stress-ROS-inflammation cycle. Importantly, the engineered ERR-HJ exhibits robust and unexpected bacterial-killing and ER-regulating performance, which furnishes a promising pathway to create biocatalytic heterojunction materials for therapeutic applications against diverse bacterial infection-associated diseases, including osteomyelitis, acne, and endocarditis (Figure 1).

15214095, 0, Downloaded from https://advanced.onlinelibrary.wiley.com/doi/10.1002/adma.75394 by Sichuan University, Wiley Online Library on [23/10/2026]. See the Terms and Conditions (https://onlinelibrary.wiley.com/terms-and-conditions) on Wiley Online Library for rules of use; OA articles are governed by the applicable Creative Commons License

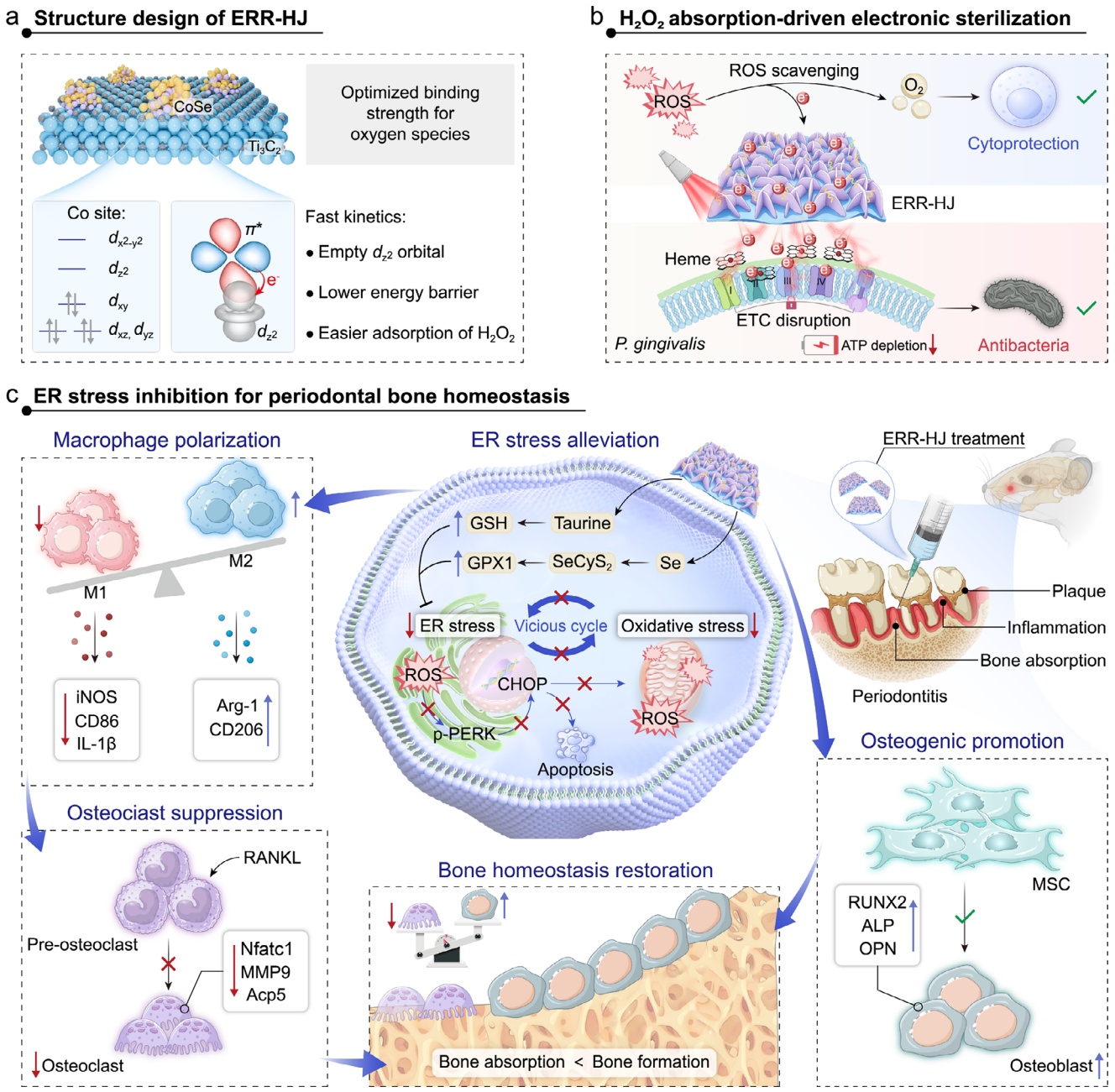


FIGURE 1 | Schematic illustration of breaking the ER stress-ROS-inflammation cycle using ERR-HJ that yields integrated antibacterial and osteoimmune regulatory functions. (a) Electronic structure optimization of the CoSe/Ti_3C_2 heterojunction. (b) H_2O_2-driven electron transfer disrupts bacterial respiration. (c) Redox–ER stress regulation promotes osteoimmune homeostasis and periodontal regeneration. Created in BioRender. Chen, W. (2026) https://BioRender.com/5mlo8qx.

2 | Results and Discussion

2.1 | ER Stress-Associated Inflammatory Microenvironment in Periodontitis and the Rational Design of ERR-HJ

Periodontitis is characterized by persistent inflammation and immune dysregulation [1]; however, the involvement of ER stress in shaping the inflammatory microenvironment remains incompletely understood. To systematically explore ER stress-associated transcriptional alterations in periodontitis, we analyzed a publicly available bulk transcriptomic dataset (GSE10334), which comprises gingival tissue samples from periodontitis patients and healthy controls. Gene set enrichment analysis (GSEA) reveals a pronounced enrichment of the protein processing within endoplasmic reticulum pathway in periodontitis samples, indicating activation of ER stress-related processes at the transcriptomic level (Figure S1a). To further quantify ER stress activity at the individual sample level, single-sample GSEA (ssGSEA) was performed, demonstrating significantly elevated ER stress scores in periodontitis compared with healthy controls (Figure S1b). Given the critical role of macrophages

15214095, 0, Downloaded from https://advanced.onlinelibrary.wiley.com/doi/10.1002/adma.75394 by Sichuan University, Wiley Online Library on [23/10/2026]. See the Terms and Conditions (https://onlinelibrary.wiley.com/terms-and-conditions) on Wiley Online Library for rules of use; OA articles are governed by the applicable Creative Commons License

in periodontal inflammation, we next evaluated macrophage-associated signatures. Analysis of M1 macrophage-related gene signatures reveals altered inflammatory macrophage responses in periodontitis (Figure S1c) [37]. Notably, correlation analysis shows a positive association between ER stress scores and M1 macrophage signatures across samples, suggesting a potential link between ER stress activation and inflammatory macrophage infiltration (Figure S1d). To validate these findings at the tissue level, immunofluorescence staining was performed in a rat model of periodontitis. ER stress markers, including the luminal chaperone GRP78 and phosphorylated PKR-like endoplasmic reticulum kinase (p-PERK), are prominently detected in $CD68^+$ macrophages within gingival tissues (Figure S1e) [9, 13]. Quantitative analysis further demonstrates an increased proportion of ER stress-positive macrophages, defined as $CD68^+GRP78^+$ or $CD68^+p\text{-}PERK^+$ cells, in periodontitis tissues (Figure S1f). In addition, the mean fluorescence intensity of GRP78 and p-PERK within $CD68^+$ macrophages is significantly elevated (Figure S1g). These findings indicate that ER stress elevation is associated with pro-inflammatory macrophage activation in periodontitis. However, whether targeted modulation of ER stress can effectively restore macrophage homeostasis and mitigate periodontitis progression remains unclear.

To address this, we rationally design an ERR-HJ to modulate the ER stress-associated inflammatory microenvironment. The fabrication process of the rationally designed ERR-HJ is illustrated in Figure 2a. This process is initiated by preparing a highly crystalline Ti_3C_2 monolayer via an ice-bath-assisted ultrasonication method (Figure S2). Guided by zeta potential analysis, the negatively charged nature of the Ti_3C_2 surface is exploited to electrostatically anchor Co^{2+} cations (Figure 2j). This initial surface enrichment serves as a crucial precursor step for the subsequent solvothermal growth of positively charged CoSe/Ti_3C_2 heterojunctions. Morphological characterizations of CoSe/Ti_3C_2 via scanning electron microscopy (SEM) and transmission electron microscopy (TEM) reveal a striking structural evolution. Pure CoSe monomers typically form micro-sized sheets (Figure S3a), while CoSe/Ti_3C_2 exhibits a dense and uniform array of CoSe nanosheets directly grown across the Ti_3C_2 templates (Figure 2b,c). The structural integrity of this well-defined 2D heterojunction is further corroborated by synergistic dynamic light scattering (DLS) and atomic force microscopy (AFM) analyses, which define a micrometric lateral scale alongside an ultrathin profile of ~10 nm (Figure S4). Crucially, energy-dispersive x-ray spectroscopy (EDS) mapping authenticates the uniformity of Ti, C, Co, and Se (Figure 2f and Figure S5).

Beyond macroscopic morphology, the atomic-level integration of the heterostructure is substantiated through crystallographic analyses. The lattice spacings in high-resolution TEM (HRTEM) of CoSe/Ti_3C_2 are determined to be approximately 0.19 and 0.26 nm, which agree well with the (110) plane of CoSe and the (100) plane of Ti_3C_2 (Figure 2d,e). These observations are in excellent agreement with the selected area electron diffraction (SAED) pattern (Figure S6). The x-ray diffraction (XRD) pattern of CoSe/Ti_3C_2 exhibits the coexistence of distinct diffraction peaks from both CoSe and Ti_3C_2. Especially, the formation of CoSe/Ti_3C_2 induces a conspicuous leftward shift in the (002) reflection of Ti_3C_2 (Figure 2k). Further compositional verification by Raman spectroscopy (Figure S7) and thermogravimetric (TG) analysis (Figure 2l) confirms the phase purity and establish an optimal CoSe to Ti_3C_2 mass ratio of approximately 4:1.

To unravel the electronic interactions underlying the CoSe/Ti_3C_2 heterostructure, x-ray photoelectron spectroscopy (XPS) was employed (Figure S8). Notably, upon interfacial contact, the Ti 2*p* spectra of the heterojunction exhibit a distinct negative shift toward lower binding energy (Figure 2g), indicating an accumulation of electron density on the Ti_3C_2 substrate. Synchronously, the Se 3*d* spectra display a corresponding shift toward higher binding energy (Figure 2h). Concurrently with these interfacial elemental modulations, the Co 2*p* core levels also demonstrate a pronounced shift toward higher binding energy compared to pristine CoSe (Figure 2i). This orchestrated binding energy shift provides compelling evidence for spontaneous electron migration from CoSe to Ti_3C_2 substrate, thereby establishing a robust, directional interfacial electric field (IEF). Concurrently, this electron transfer from CoSe to Ti_3C_2 induces a redistribution of cobalt oxidation states, reducing Co^{2+} from 76.9% to 74.2% and elevating Co^{3+} from 23.1% to 25.8% in the CoSe/Ti_3C_2. Such electronic reconfiguration and multivalent state optimization are anticipated to significantly amplify the electron-accepting capability of the heterojunction.

To further decipher the interfacial electronic transfer between CoSe and Ti_3C_2, we systematically mapped the band alignment of the CoSe/Ti_3C_2 heterojunction. Density functional theory (DFT) calculations were first conducted to probe theoretical support for the simulated structures (Figure S9). As illustrated in the calculated band structures (Figure S10), CoSe exhibits a semiconducting nature with a narrow bandgap of 1.145 eV, whereas Ti_3C_2 displays a typical metallic character with a bandgap of 0 eV, characterized by the continuous electronic states crossing the Fermi level (E_f). Notably, upon the formation of the heterojunction, the CoSe/Ti_3C_2 maintains a vanishing bandgap (E_g = 0 eV). This metallic-like behavior of the heterojunction is further corroborated by the enriched electronic density of states (DOS) at E_f (Figure S11). The high density of states at the E_f indicates enhanced conductivity and abundant mobile electrons, providing a formidable physical foundation for the rapid electron transfer capability to pathogenic bacteria. As shown in Figure S12, DFT calculations reveal the work function (Φ) of 4.315 eV for CoSe, which is notably smaller than that of Ti_3C_2 (5.063 eV). Therefore, upon contact between CoSe and Ti_3C_2, a Schottky heterojunction is established, driving electron migration from CoSe with a higher E_f toward Ti_3C_2 with a lower E_f until interfacial equilibrium is achieved within the CoSe/Ti_3C_2 heterojunction, consistent with the XPS analysis. To visualize this interfacial interaction at the atomic scale, the differential charge density was calculated (Figure S13). A clear charge redistribution is observed at the heterojunction interface, where an obvious electron depletion occurs at the CoSe side, accompanied by significant electron accumulation at the Ti_3C_2 side. From the UV–vis diffuse reflectance spectra (DRS) calculated by the Kubelka–Munk formula, the band gap narrows from 1.09 eV in CoSe to 0.75 eV after the formation of CoSe/Ti_3C_2, which exhibits a trend consistent with the DFT calculations (Figure S14). The diminished band gap proves advantageous in augmenting the generation of photogenerated electrons under equivalent irradiation. Moreover, the valence band maximum (VBM) positions of CoSe and CoSe/Ti_3C_2 are determined by the XPS valence band spectrum to be 0.179 and

15214095, 0, Downloaded from https://advanced.onlinelibrary.wiley.com/doi/10.1002/adma.75394 by Sichuan University, Wiley Online Library on [23/10/2026]. See the Terms and Conditions (https://onlinelibrary.wiley.com/terms-and-conditions) on Wiley Online Library for rules of use; OA articles are governed by the applicable Creative Commons License

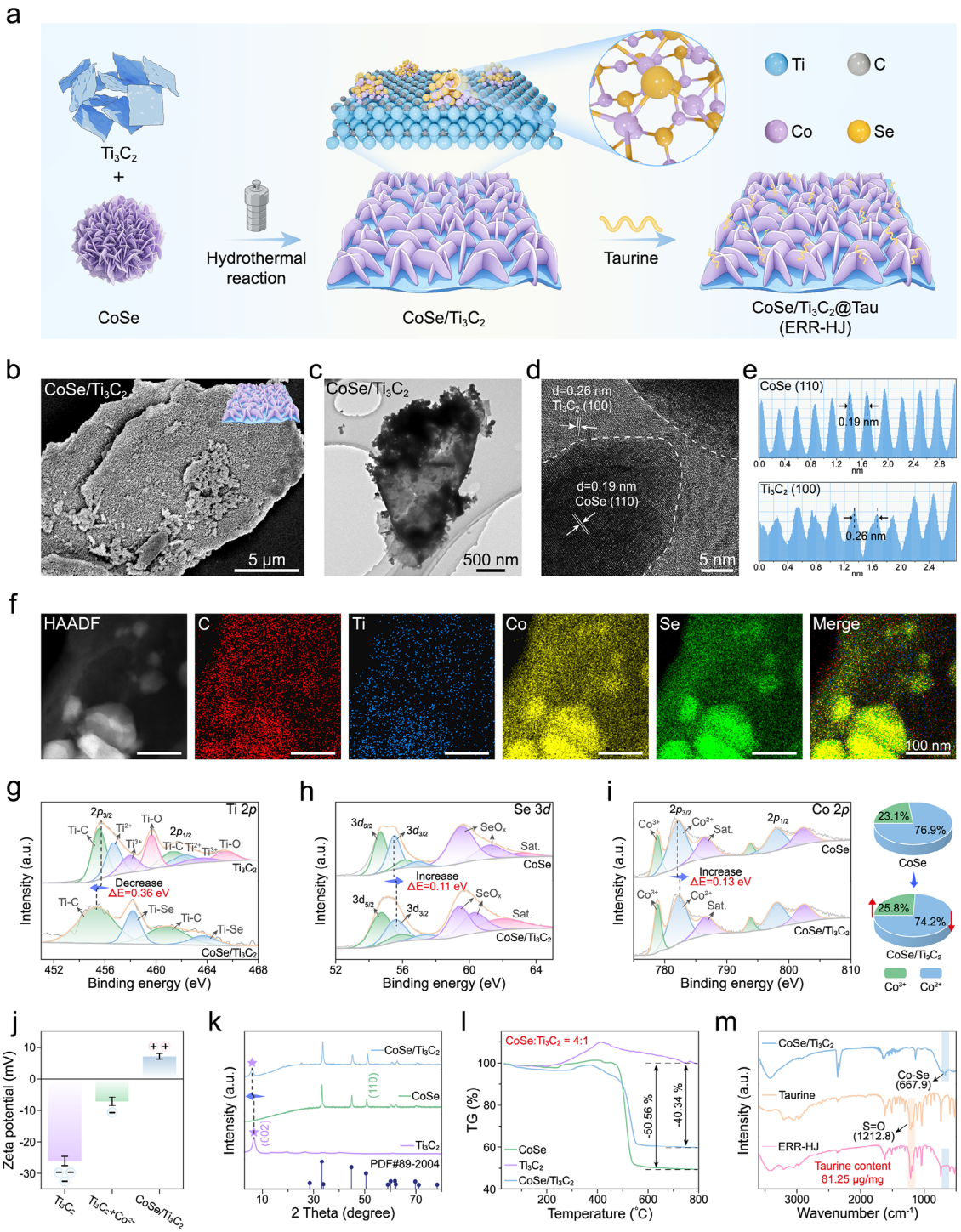


FIGURE 2 | Synthesis and characterization of CoSe/Ti_3C_2 heterojunction and ERR-HJ. (a) Schematic diagram of the construction of CoSe/Ti_3C_2 and ERR-HJ, created in BioRender. Chen, W. (2026) https://BioRender.com/5mlo8qx. (b–e) SEM, TEM, HRTEM images and lattice spacing measurements of CoSe/Ti_3C_2. (f) HAADF and elemental mapping of CoSe/Ti_3C_2. (g–i) High-resolution XPS spectra of Ti 2*p* for Ti_3C_2 and CoSe/Ti_3C_2, Se 3*d* and Co 2*p* for CoSe and CoSe/Ti_3C_2. (j) Zeta potential of Ti_3C_2, Ti_3C_2+Co^{2+}, and CoSe/Ti_3C_2 ($n = 3$ independent replicates, all data are presented as mean ± SD). (k) XRD patterns and (l) TG analysis of CoSe, Ti_3C_2, and CoSe/Ti_3C_2. (m) FT-IR spectra of CoSe/Ti_3C_2, Taurine, and ERR-HJ.

0.114 eV, respectively (Figure S15). By incorporating the samples' work function, the valence band potential (VB) is then converted to the normal hydrogen electrode (NHE) scale, yielding values of −4.50 and −4.09 eV, respectively. The conduction band position (CB) is calculated as CB = VB—E_g. Combining the above results, it can be inferred that the electron transfer at the CoSe/Ti_3C_2 Schottky heterojunction interface occurs as illustrated in Figure S16. Due to the difference in work function between CoSe and Ti_3C_2, the interfacial contact causes E_f alignment and conduction band bending. Consequently, a Schottky barrier is established at the semiconductor-metal interface, facilitating directional charge transfer.

15214095, 0, Downloaded from https://advanced.onlinelibrary.wiley.com/doi/10.1002/adma.75394 by Sichuan University, Wiley Online Library on [23/10/2026]. See the Terms and Conditions (https://onlinelibrary.wiley.com/terms-and-conditions) on Wiley Online Library for rules of use; OA articles are governed by the applicable Creative Commons License

Steady-state photoluminescence (PL) spectra and photoelectrochemical measurements were subsequently employed to investigate the charge-separation behavior of CoSe/Ti_3C_2. The significantly quenched PL emission relative to pure CoSe demonstrates the efficient inhibition of electron–hole recombination in the heterostructure (Figure S17a). Moreover, CoSe/Ti_3C_2 consistently exhibits the highest photocurrent and photovoltage compared to pristine CoSe during the transient photocurrent test and surface photovoltage test (Figure S17b,c). These disparities can be attributed to the superior localized surface plasmon resonance (LSPR) effect of Ti_3C_2 MXene that facilitates charge separation and transfer in CoSe/Ti_3C_2 [38]. To further elucidate the LSPR effect on photocurrent, 3D finite element simulations were performed, showing the electric field distribution of CoSe/Ti_3C_2 under 808 nm NIR irradiation, with nanospheres representing CoSe nanoparticles and the bottom layer representing Ti_3C_2 (Figure S18). Under NIR irradiation, the internal electric field inside the Ti_3C_2 beneath the CoSe within the heterojunction structure reaches 6.78 V/m, indicating that heterojunction formation facilitates electron generation in the connecting region, while the LSPR effect of Ti_3C_2 enhances the energetic activity of electrons, enabling efficient excitation and transfer to bacteria.

Finally, to endow the heterojunction with specific biological functionality, the architecture is covalently functionalized with taurine using mussel-inspired chemistry via Michael addition and Schiff base reactions between the amine groups of taurine and the quinone groups of polydopamine (PDA), yielding the final ERR-HJ. This modification preserves the morphological integrity of the parent composite (Figure S3b). The successful integration of taurine was probed by Fourier transform infrared spectroscopy (FT-IR), wherein the emergence of the S═O asymmetric stretching vibration at 1212.8 cm^{-1} confirms the robust molecular grafting alongside the characteristic Co—Se bond at 667.9 cm^{-1} (Figure 2t). Subsequent quantification via the ninhydrin assay reveals an exceptional taurine loading capacity of 81.25 μg/mg (Figure S19). Furthermore, taurine release from ERR-HJ in PBS at 37°C exhibited an initial rapid phase (~57.3% on day 1), followed by a sustained release profile, with cumulative release reaching ~90.5% by day 7 (Figure S20). The release behavior of Se from ERR-HJ was further evaluated by inductively coupled plasma-mass spectrometry (ICP-MS). Se release increases over time, reaching 7.82 μg/mL in PBS and 8.82 μg/mL in the presence of H_2O_2 at 48 h (Figure S21), with moderately enhanced release under oxidative conditions. Through the successful loading of taurine, a highly enriched bioactive interface is established, not only shielding the heterojunction from direct host contact but also providing a functional platform for subsequent intracellular ER-stress targeting and microenvironment modulation.

2.2 | Experimental and Theoretical Analysis on Antioxidant Activities

Given the imperative role of ROS in the progression of periodontitis, we systematically evaluated the antioxidant efficacy of CoSe/Ti_3C_2 as a multifunctional scavenger (Figure 3a). Primarily, the efficient clearance of hydroxyl radicals (·OH) and superoxide anions ($\cdot O_2^-$) was qualitatively verified via electron paramagnetic resonance (EPR) measurements adopting 5,5-Dimethyl-1-pyrroline N-oxide (DMPO) as the spin trap reagent. The markedly attenuated signal intensities reveal that CoSe/Ti_3C_2 effectively consumes both ·OH and $\cdot O_2^-$ (Figure 3b,d). Quantitative analyses further demonstrate that CoSe/Ti_3C_2 can remove 80.8% of ·OH within 5 min, which is superior to that of CoSe (Figure 3c and Figure S22). The $\cdot O_2^-$ decomposition efficiency reaches 82.7%, surpassing the 65.3% observed for CoSe (Figure 3e and Figure S23). For the H_2O_2 scavenging process, the CoSe/Ti_3C_2 can dramatically reduce H_2O_2 concentration (~71% at 30 min), which remarkably outperforms the bare CoSe (Figure 3f and Figure S24). Meanwhile, O_2 generation shows a similar trend. CoSe/Ti_3C_2 significantly increases O_2 concentration from 4.5 to 52.2 mg/L at 5 min, which is much faster than CoSe does (Figure 3g). To decipher the catalytic superiority, steady-state kinetic parameters were determined using Lineweaver–Burk plots (Figure S25). Compared to CoSe, CoSe/Ti_3C_2 exhibits a relatively smaller Michaelis-Menten constant (K_m) of 11.6 mM, indicating its exceptional substrate affinity. Michaelis–Menten kinetic analysis further indicates that CoSe/Ti_3C_2 possesses an enhanced maximum reaction velocity (V_{max}, a steady-state kinetic parameter) of 29.1 μM s^{-1}, representing a 1.5-fold increase compared with CoSe. Since the apparent V_{max} can be influenced by the accessible catalytic surface, we further estimated the electrochemically active surface area (ECSA) from the double-layer capacitance (C_{dl}) (Figure S26). Interestingly, CoSe/Ti_3C_2 exhibited a substantially smaller estimated ECSA than CoSe (24.5 vs. 84.25 cm^2), whereas its ECSA-normalized V_{max} increased from approximately 0.23 to 1.19 μM s^{-1} cm^{-2}. After normalization to the amounts of Co catalytic centers, CoSe/Ti_3C_2 exhibits a turnover number (TON, maximum number of converting substrates per unit catalytic sites) of 1.4 s^{-1}, which is approximately 2.3 times higher than that of CoSe (Figure 3h). For comparison with previously reported catalase (CAT)-mimetic materials, TON rather than absolute V_{max} was used as the primary normalized kinetic parameter. Among the systems summarized in Table S1, CoSe/Ti_3C_2 exhibits the highest TON values, supporting its efficient utilization of catalytic sites (Figure 3i and Table S1).

To further validate its broad-spectrum efficacy, we explored the scavenging potential of the CoSe/Ti_3C_2 against reactive nitrogen species (RNS) and standardized synthetic radicals. EPR measurements confirm the efficient ablation of nitric oxide (NO) by CoSe/Ti_3C_2, evidenced by a markedly attenuated signal intensity (Figure S27). Furthermore, CoSe/Ti_3C_2 achieves a 41.3% scavenging efficiency against peroxynitrite ($ONOO^-$), a highly cytotoxic RNS prevalent in inflammatory microenvironments (Figure S28). Then, CoSe/Ti_3C_2 was tested against standardized synthetic radicals, and exhibited robust scavenging efficacies of 82.2% for $ABTS^{\cdot+}$ and 73.7% for DPPH·(Figures S29 and S30). Finally, the total antioxidant capacity was benchmarked via the Trolox-equivalent antioxidant capacity assay, where the CoSe/Ti_3C_2 yields a value of 0.182 mM at a concentration of 50 μg/mL, slightly surpassing the capability of CoSe (Figure S31).

Intriguingly, Kelvin probe force microscopy (KPFM) was performed to intuitively visualize the surface-enriched electrons on the CoSe/Ti_3C_2 following electron uptake from H_2O_2. As depicted in Figure 3j,k, the potential difference decreases sharply from 197.5 mV for pristine CoSe/Ti_3C_2 to 67.1 mV after exposure to H_2O_2. Zeta potential analysis further demonstrates that CoSe/Ti_3C_2 gains more negative surface charge after H_2O_2 exposure, suggesting electron accumulation and supporting an

15214095, 0, Downloaded from https://advanced.onlinelibrary.wiley.com/doi/10.1002/adma.75394 by Sichuan University, Wiley Online Library on [23/10/2026]. See the Terms and Conditions (https://onlinelibrary.wiley.com/terms-and-conditions) on Wiley Online Library for rules of use; OA articles are governed by the applicable Creative Commons License

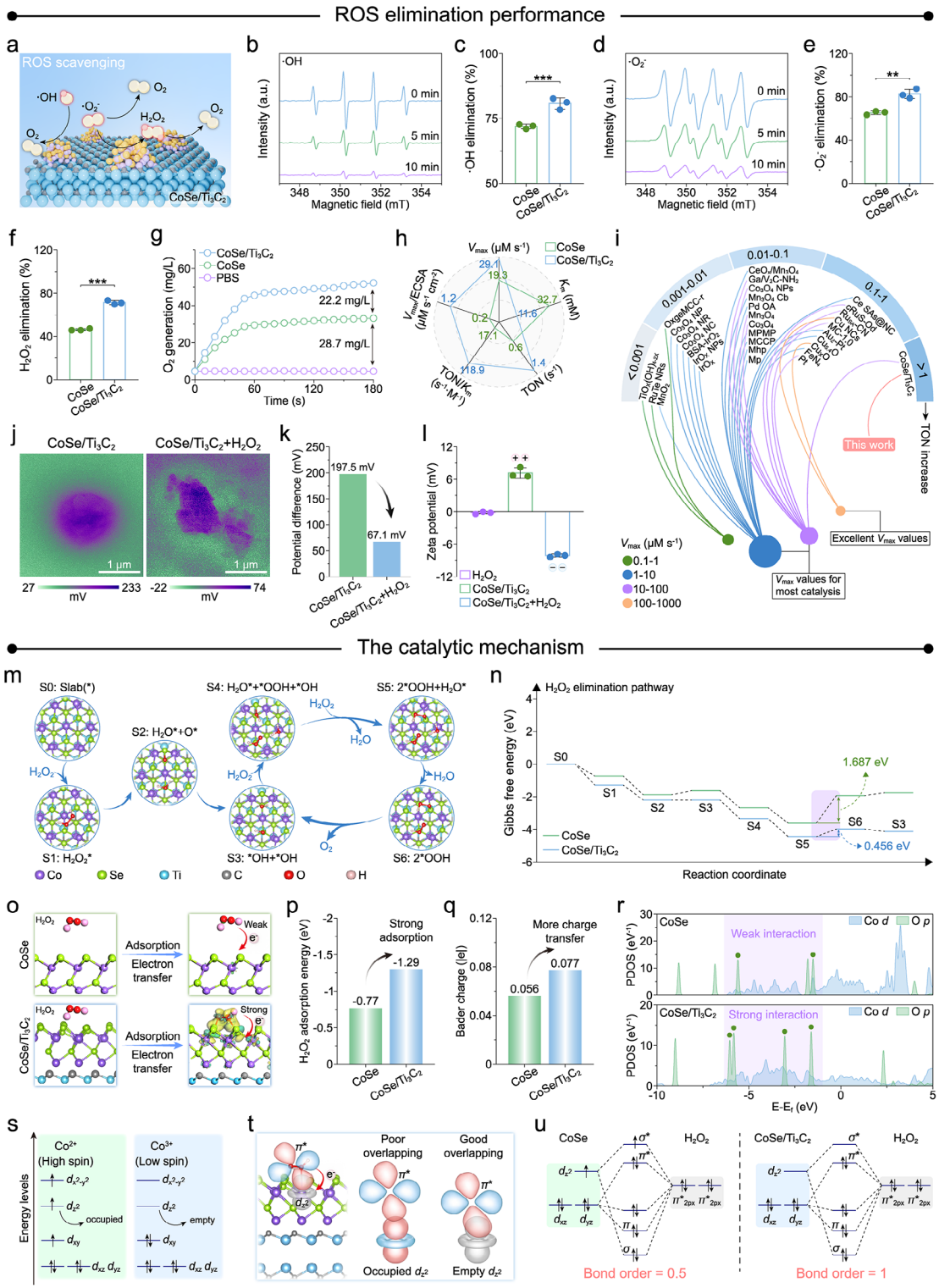


FIGURE 3 | Experimental evaluation and theoretical calculation of antioxidant capacity. (a) Schematic diagram of the heterojunction-mediated ROS scavenging, created in BioRender. Chen, W. (2026) https://BioRender.com/5mlo8qx. (b) EPR spectra and (c) elimination ratio of ·OH ($n = 3$ independent replicates). (d) EPR spectra and (e) elimination ratio of O_2^- ($n = 3$ independent replicates). (f) H_2O_2 elimination ratio for different materials ($n = 3$ independent replicates). (g) The produced O_2 concentration was measured by a dissolved oxygen meter in the presence of heterojunctions and H_2O_2. (h) V_{max}, V_{max}/ECSA, K_m, TON, and TON/K_m values of CoSe and CoSe/Ti_3C_2. (i) Comparative analysis of the V_{max} and TON with previously reported antioxidant materials. (j) KPFM potential images of CoSe/Ti_3C_2 and CoSe/Ti_3C_2+H_2O_2, and (k) corresponding surface potential. (l) Zeta potential of CoSe/Ti_3C_2 and CoSe/Ti_3C_2+H_2O_2 ($n = 3$ independent replicates). (m) H_2O_2 decomposition reactive pathways and (n) Gibbs free energy diagram of CoSe and CoSe/Ti_3C_2. (o) Differential charge density analysis of the adsorption of H_2O_2 on CoSe and CoSe/Ti_3C_2 (cyan and yellow isosurfaces represent electron accumulation and depletion, respectively). (p) Adsorption energy and (q) calculated Bader charge of CoSe and CoSe/Ti_3C_2 with the adsorption of H_2O_2. (r) PDOS (where Co corresponds to the 3d orbital and O signal represents the 2p orbital) of CoSe and CoSe/Ti_3C_2 with the adsorption of H_2O_2.

15214095, 0, Downloaded from https://advanced.onlinelibrary.wiley.com/doi/10.1002/adma.75394 by Sichuan University, Wiley Online Library on [23/10/2026]. See the Terms and Conditions (https://onlinelibrary.wiley.com/terms-and-conditions) on Wiley Online Library for rules of use; OA articles are governed by the applicable Creative Commons License

electron-accepting mechanism for H_2O_2 scavenging (Figure 3l). Collectively, the above results demonstrate that the electrons absorbed from H_2O_2 elevate the local electron density and modulate the surface potential. Subsequently, a robust electron transfer can be induced via the LSPR effect to achieve efficient bacterial inactivation, which would be systematically validated in the subsequent antibacterial assays.

Subsequently, computational analyses using DFT were carried out to elucidate the fundamental correlation between the Co centers and their catalytic efficacy in H_2O_2 decomposition. The catalytic mechanisms of the H_2O_2 decomposition reaction via a heterolytic two-electron transfer pathway are illustrated in Figure 3m and Figures S32 and S33. The reaction energy barriers are about 1.687 eV for CoSe and 0.456 eV for CoSe/Ti_3C_2, indicating that interfacial electron transfer from CoSe to Ti_3C_2 optimizes the *d* orbital energy level of Co, augments H_2O_2 adsorption, and consequently lowers the energy barrier (Figure 3n). Adsorption energy (E_{ads}) calculations show that CoSe/Ti_3C_2 has a stronger interaction with H_2O_2 than CoSe, favoring the activation of H_2O_2 (Figure 3p). Compared to the monolithic materials, the CoSe/Ti_3C_2 induces a more pronounced elongation of the O—O and H—O bonds and significant geometric distortion of the H—O—O bond angle in the adsorbed H_2O_2 molecule (Figure S34). Then, the charge density difference was computed to study the strong adsorption of H_2O_2 on the samples. Figure 3o shows that the strong adsorption of reactants induces significant charge transfer from H_2O_2 to CoSe/Ti_3C_2 through the electron-donation process. The empty d_{z2} orbitals of Co 3*d* can accept lone-pair electrons of H_2O_2. The precise charge transfer quantity was further determined through Bader population analysis (Figure 3q). Moreover, as presented in Figure 3r, the analysis of partial density of states (PDOS) reveals that a strong d–p orbital coupling occurs at the interface, characterized by the significant overlap between the Co 3*d* in CoSe/Ti_3C_2 and the O 2*p* of H_2O_2. Consistently, the calculated d-band center (ε_d) provides a quantitative descriptor for the aforementioned orbital coupling (Figure S35). The ε_d of Co is markedly elevated toward the E_f, shifting from −1.71 eV (CoSe) to −1.54 eV (CoSe/Ti_3C_2), which reduces the occupancy of antibonding orbitals during H_2O_2 adsorption, thereby significantly strengthening the interfacial binding and promoting catalytic activation.

Molecular orbital theory was further employed to analyze the orbital interaction of Co and H_2O_2. The CoSe component is modeled in its stable hexagonal structure (space group $P6_3/mmc$), with Co atoms occupying octahedral interstitial sites. According to the crystal field theory, the octahedral coordination environment causes the Co *d* orbitals to split into the e_g and t_{2g} energy levels due to the electrostatic repulsion from the surrounding Se ligands (Figure S36). Truncation of the surface Se atom lowers the octahedral symmetry, leading to a downward shift in the energy levels of the d_{xz}, d_{yz}, and d_{z2} orbitals and correspondingly providing additional stabilization energy (Figure S37). Typically, the redistribution of electrons triggers the evolution of the 3*d* spin state. In the pristine CoSe lattice, Co^{2+} (d^7) typically adopts a high-spin configuration due to the relatively weak crystal field provided by the Se ligands. However, the interfacial charge transfer in the heterojunction from CoSe to Ti_3C_2 elevates the oxidation state of Co to Co^{3+} (d^6). The increased charge of Co^{3+} leads to a concomitant increase in the crystal field splitting energy (Δ), triggering a transition to a low-spin state. This spin-state transition results in a completely vacant d_{z2} orbital (Figure 3s). Owing to the symmetry mismatch, the interactions between the d_{x2-y2} and d_{xy} orbitals of Co and the π antibonding orbitals (π^*) orbitals of H_2O_2 are negligible. During H_2O_2 adsorption and activation, the π^*_{2px} and π^*_{2py} bonds of H_2O_2 can interact with the frontier molecular orbitals (FMOs) of CoSe/Ti_3C_2, because these orbitals are not fully occupied (Figure S38). The schematic orbital interaction illustration shows that the charge-occupied Co $3d_{z2}$ orbital in CoSe displays poor overlap with π^* of the adsorbed H_2O_2. While the empty Co $3d_{z2}$ orbital near the Fermi level in CoSe/Ti_3C_2 presents no interference, thus giving the π^* orbital the possibility to form strong sigma bonds with the Co $3d_{z2}$ orbital in CoSe/Ti_3C_2, as shown in Figure 3t. Bond order calculations were conducted to provide a quantitative descriptor of the interfacial chemical bond interaction stability (Figure 3u). Molecular orbital analysis shows that the vacant d_{z2} orbital in CoSe/Ti_3C_2 results in lower electron occupancy of the antibonding orbitals upon interaction between Co and H_2O_2. This leads to a pronounced elevation of the bond order from 1.5 to 2.0.

2.3 | In Vitro Antibacterial Performance Under NIR

Among the diverse subgingival microbiome, the Gram-negative obligate anaerobe *Porphyromonas gingivalis* (*P. gingivalis*) is widely recognized as the keystone pathogen responsible for initiating immune evasion and severe periodontal tissue destruction [1]. Concurrently, *Staphylococcus aureus* (*S. aureus*), a representative Gram-positive pathogen, is frequently implicated in refractory periodontal infections and complex oral dysbiosis [39]. Therefore, to systematically validate the broad-spectrum antibacterial efficacy of the CoSe/Ti_3C_2, *P. gingivalis* and *S. aureus* are selected as the respective model strains for antimicrobial assessments. We first evaluated the antibacterial activity of different materials against planktonic *P. gingivalis* and *S. aureus*. Live/Dead staining was conducted on five groups (PBS, H_2O_2, CoSe/Ti_3C_2, CoSe/Ti_3C_2+H_2O_2 and ERR-HJ+H_2O_2) with or without NIR irradiation to assess bacterial viability (Figure 4a,b and Figure S39), revealing the strongest red fluorescence in the CoSe/Ti_3C_2+H_2O_2 and ERR-HJ+H_2O_2 groups and confirming their pronounced antibacterial potency under NIR laser stimulation. SEM was also used to investigate the morphological changes of treated bacteria (Figure 4c and Figure S40). Severe disruption of bacterial membranes is observed in the CoSe/Ti_3C_2+H_2O_2 and ERR-HJ+H_2O_2 groups, marked by green arrows, while the other groups exhibit

(s) Diagram of d orbital and energy level for Co^{2+} and Co^{3+}. (t) Schematic orbital interaction illustration between π^* orbital in H_2O_2 and the charge occupied d_{z2} orbital in Co^{2+} and empty d_{z2} orbital in Co^{3+}. (u) Molecular orbital diagrams between H_2O_2 and Co 3*d* of CoSe or CoSe/Ti_3C_2. All data are presented as mean ± SD. One-way ANOVA followed by Tukey's post hoc test was used. Significant differences between groups were indicated as $^{***}p < 0.001$, $^{**}p < 0.01$, $^{*}p < 0.05$, and ns represents not significant.

15214095, 0, Downloaded from https://advanced.onlinelibrary.wiley.com/doi/10.1002/adma.75394 by Sichuan University, Wiley Online Library on [23/10/2026]. See the Terms and Conditions (https://onlinelibrary.wiley.com/terms-and-conditions) on Wiley Online Library for rules of use; OA articles are governed by the applicable Creative Commons License

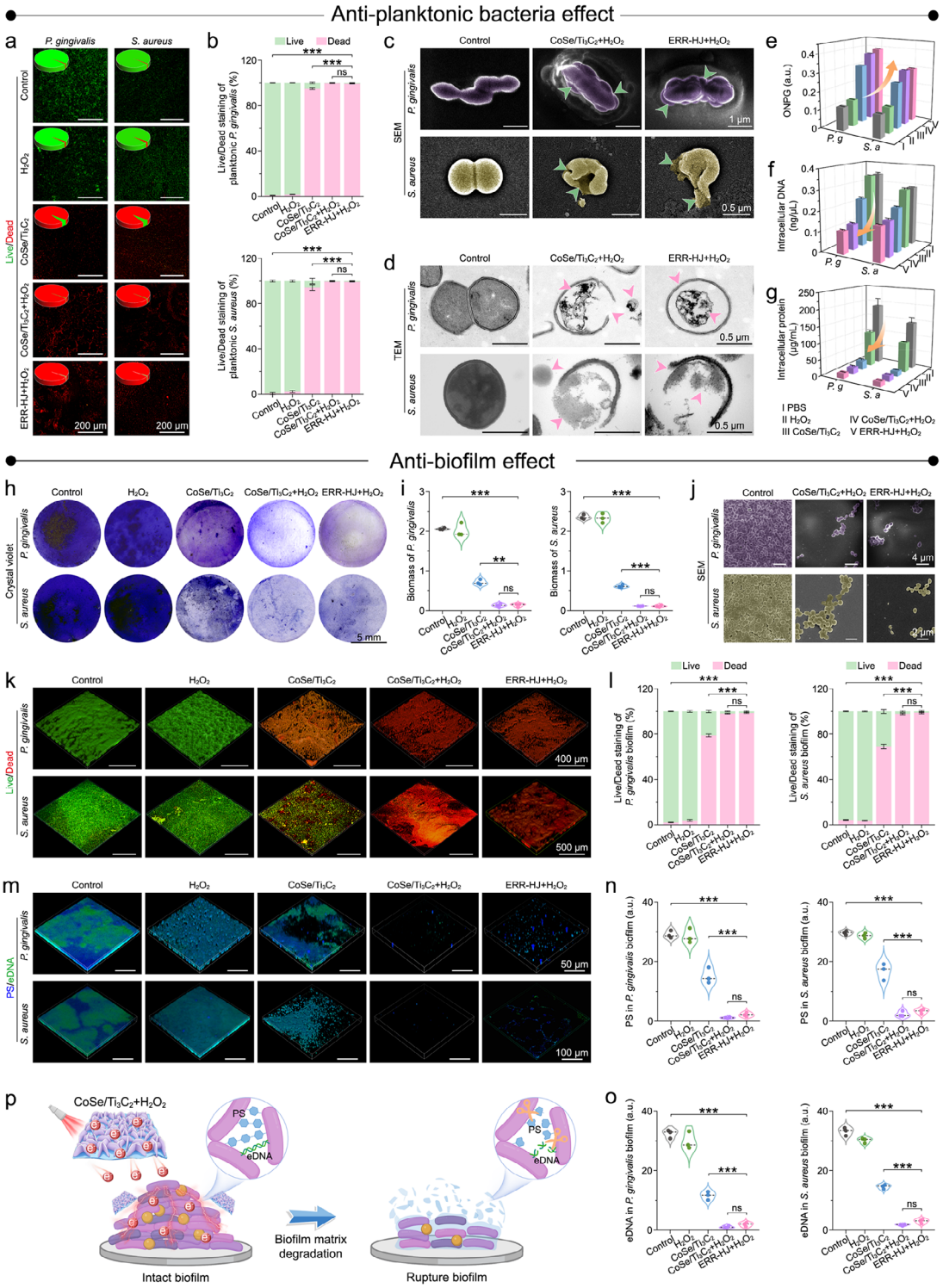


FIGURE 4 | In vitro antibacterial performance under NIR. (a) Live/Dead staining fluorescence images of planktonic *P. gingivalis* and *S. aureus*, and (b) corresponding Live/Dead ratios ($n = 3$ independent replicates). (c) SEM and (d) TEM morphologies of planktonic *P. gingivalis* and *S. aureus* after treatments (arrows indicate membrane rupture and cytoplasmic leakage). (e–g) Assessment of membrane permeability and quantification of intracellular DNA and protein contents in *P. gingivalis* and *S. aureus* following various treatments ($n = 3$ independent replicates). (h) Crystal violet staining and (i) associated quantitative analysis of *P. gingivalis* and *S. aureus* biofilms ($n = 3$ independent replicates). (j) SEM morphologies of treated biofilms. (k) 3D fluorescence images from Live/Dead staining of *P. gingivalis* and *S. aureus* biofilms and (l) corresponding ratios ($n = 3$ independent replicates). (m) Staining of PS and eDNA in the biofilm EPS and (n,o) corresponding fluorescence intensity statistics ($n = 3$ independent replicates). (p) Schematic illustration of the biofilm eradication procedure, created in BioRender. Chen, W. (2026) https://BioRender.com/5mlo8qx. All data are presented as mean ± SD. One-way ANOVA followed by Tukey's post hoc test was used. Significant differences between groups were indicated as $^{***}p < 0.001$, $^{**}p < 0.01$, $^{*}p < 0.05$, and ns represents not significant.

15214095, 0, Downloaded from https://advanced.onlinelibrary.wiley.com/doi/10.1002/adma.75394 by Sichuan University, Wiley Online Library on [23/10/2026]. See the Terms and Conditions (https://onlinelibrary.wiley.com/terms-and-conditions) on Wiley Online Library for rules of use; OA articles are governed by the applicable Creative Commons License

regular coccobacillus morphology of *P. gingivalis* and spherical shapes of *S. aureus*. TEM analysis was further performed to examine the ultrastructural alterations of bacterial membranes and intracellular components after treatment (Figure 4d). Compared to the PBS group, CoSe/Ti_3C_2+H_2O_2 and ERR-HJ+H_2O_2 under NIR induce membrane rupture and cytoplasmic leakage (pointed out by pink arrows) in *P. gingivalis* and *S. aureus*. Subsequently, the o-nitrophenyl-*β*-D-galactopyranoside (ONPG) assay was employed as an initial indicator of alterations in bacterial membrane permeability. Under NIR irradiation, *P. gingivalis* and *S. aureus* in the CoSe/Ti_3C_2+H_2O_2 and ERR-HJ+H_2O_2 groups exhibit substantial membrane damage and markedly increased permeability (Figure 4e). Considering the potential nonspecific response of ONPG in *S. aureus*, membrane integrity was further evaluated by Hoechst 33342/PI fluorescence staining. Consistent with the ONPG and TEM results, markedly increased PI fluorescence was observed after CoSe/Ti_3C_2+H_2O_2 and ERR-HJ+H_2O_2 treatment in both *P. gingivalis* and *S. aureus* (Figure S41), further confirming the disruption of bacterial membrane integrity. The massive depletion of intracellular DNA and proteins in the NIR-activated CoSe/Ti_3C_2+H_2O_2 and ERR-HJ+H_2O_2 group underscores a multifaceted bactericidal cascade (Figure 4f,g). This loss is associated with increased membrane permeability and impaired energy metabolism, which together compromise bacterial structural and metabolic integrity. Notably, ERR-HJ+H_2O_2 retained antibacterial activity comparable to CoSe/Ti_3C_2+H_2O_2, indicating that taurine functionalization did not compromise the antibacterial efficacy of the heterojunction. Within the tested range of 0–20 μM, CFU measurements showed effective bacterial inhibition from 5 μM onward for both *P. gingivalis* and *S. aureus* (Figure S42).

Notably, periodontal pathogens predominantly exist in biofilm form, which provides a protective barrier and markedly enhances bacterial resistance and survival, leading to persistent infection [40]. Therefore, anti-biofilm assays were carried out on *P. gingivalis* and *S. aureus* biofilms to accurately evaluate the antibacterial efficacy. Crystal violet staining (Figure 4h,i and Figure S43) and SEM (Figure 4j and Figure S44) reveal that the biofilms treated with CoSe/Ti_3C_2+H_2O_2 and ERR-HJ+H_2O_2 under NIR show reduced staining and disrupted morphology, reflecting pronounced antibiofilm activity. Furthermore, 3D Live/Dead confocal laser scanning microscopy (CLSM) reveals that the CoSe/Ti_3C_2+H_2O_2 and ERR-HJ+H_2O_2-treated biofilms present the highest proportions of dead bacteria with almost no live bacteria, whereas the other groups still retain abundant live bacteria (Figure 4k,l and Figure S45). Bacteria within biofilms secrete extracellular polymeric substances (EPS) to shield them from host defenses and external bactericidal agents, thereby protecting themselves from clearance and sustaining biofilm-associated infections [41]. Polysaccharides (PS) and extracellular DNA (eDNA), the key components of EPS, were simultaneously assessed in each group using dual staining with Calcofluor White M2R and SYBR Green to investigate potential anti-biofilm mechanisms (Figure 4m and Figure S46). Quantitative analysis reveals that CoSe/Ti_3C_2+H_2O_2 and ERR-HJ+H_2O_2 treatments significantly suppress both eDNA and PS within the biofilm under NIR, as evidenced by the marked reduction in fluorescence intensity (Figure 4n,o). These results indicate that the electron transfer process specifically targets key biofilm components such as PS and eDNA, facilitating the disintegration of the biofilm architecture (Figure 4p). Consistently, ERR-HJ+H_2O_2 exhibited antibiofilm activity comparable to that of CoSe/Ti_3C_2+H_2O_2. Nevertheless, the single-species biofilm models used here do not fully reproduce the polymicrobial complexity of periodontal biofilms in vivo. Future studies using defined multispecies or patient-derived oral biofilm models will be necessary to further evaluate the community-level antibacterial efficacy and ecological effects of ERR-HJ. Intracellular ROS levels in treated bacteria and biofilms under NIR irradiation were evaluated. The results reveal nearly undetectable green fluorescence across almost all groups, with only a marginal fluorescence signal observed in the H_2O_2 group (Figure S47). This substantiates that the exceptional antibacterial potency of CoSe/Ti_3C_2 is independent of ROS generation. Under the 808 nm NIR conditions, the temperature remained below 40°C throughout irradiation (Figure S48), indicating a limited contribution from photothermal heating [42, 43].

2.4 | Heme-Mediated Extracellular Electron Transfer From CoSe/Ti_3C_2 to *P. gingivalis* Inducing Respiratory Collapse

To evaluate whether the CoSe/Ti_3C_2 heterojunction could establish direct electronic communication with *P. gingivalis*, we first examined the interfacial electrochemical behavior. Cyclic voltammetry (CV) reveals that the redox current is markedly enhanced after the introduction of *P. gingivalis* and is further increased in the presence of H_2O_2 (Figure 5a). The maximum current response increases from 2.20 mA for CoSe/Ti_3C_2 alone to 3.11 mA after *P. gingivalis* addition and further to 4.24 mA in the CoSe/Ti_3C_2+H_2O_2+*P. gingivalis* group, indicating progressively more active interfacial charge exchange. Electrochemical impedance spectroscopy reveals a gradual reduction in the Nyquist semicircle diameter from CoSe/Ti_3C_2 to CoSe/Ti_3C_2+H_2O_2+*P. gingivalis*, demonstrating decreased charge-transfer resistance after bacterial engagement (Figure 5b and Table S2). Polarization analysis further supports this conclusion (Figure 5c). Linear sweep voltammetry (LSV) curves of CoSe/Ti_3C_2+H_2O_2+*P. gingivalis* exhibit the maximum dynamic current density (−0.28 mA/cm^2) at −0.1 V, confirming a synergistic interaction that promotes interfacial electron transfer from CoSe/Ti_3C_2 to bacterial cells. The corresponding Tafel slopes of CoSe/Ti_3C_2, CoSe/Ti_3C_2+*P. gingivalis* and CoSe/Ti_3C_2+H_2O_2+*P. gingivalis* are 552.2, 281.22, and 178.98 mV $decade^{-1}$, respectively (Figure 5d), with the reduced slope indicating enhanced electron transfer. To verify the electron-donating role of CoSe/Ti_3C_2+H_2O_2 in electron-mediated antibacterial activity, NH_4Cl was employed as a classical electron quencher in plate-counting assays. As displayed in Figure 5e, in the absence of NH_4Cl, CoSe/Ti_3C_2 significantly reduces bacterial colonies, and its combination with H_2O_2 produces the strongest antibacterial effect, yielding the lowest colony-forming units (CFU) counts. However, the introduction of NH_4Cl blocks electron transfer between CoSe/Ti_3C_2+H_2O_2 and *P. gingivalis*, compromising the antibacterial efficacy and increasing colony formation. To further corroborate the interfacial electron transfer toward pathogens, we monitored the H_2O_2 consumption and O_2 evolution kinetics in the presence of bacteria (Figure S49). Intriguingly, the introduction of *P. gingivalis* significantly accelerates the decomposition of H_2O_2, suggesting that the bacterial membrane acts as an effective electron sink. This synergy

15214095, 0, Downloaded from https://advanced.onlinelibrary.wiley.com/doi/10.1002/adma.75394 by Sichuan University, Wiley Online Library on [23/10/2026]. See the Terms and Conditions (https://onlinelibrary.wiley.com/terms-and-conditions) on Wiley Online Library for rules of use; OA articles are governed by the applicable Creative Commons License

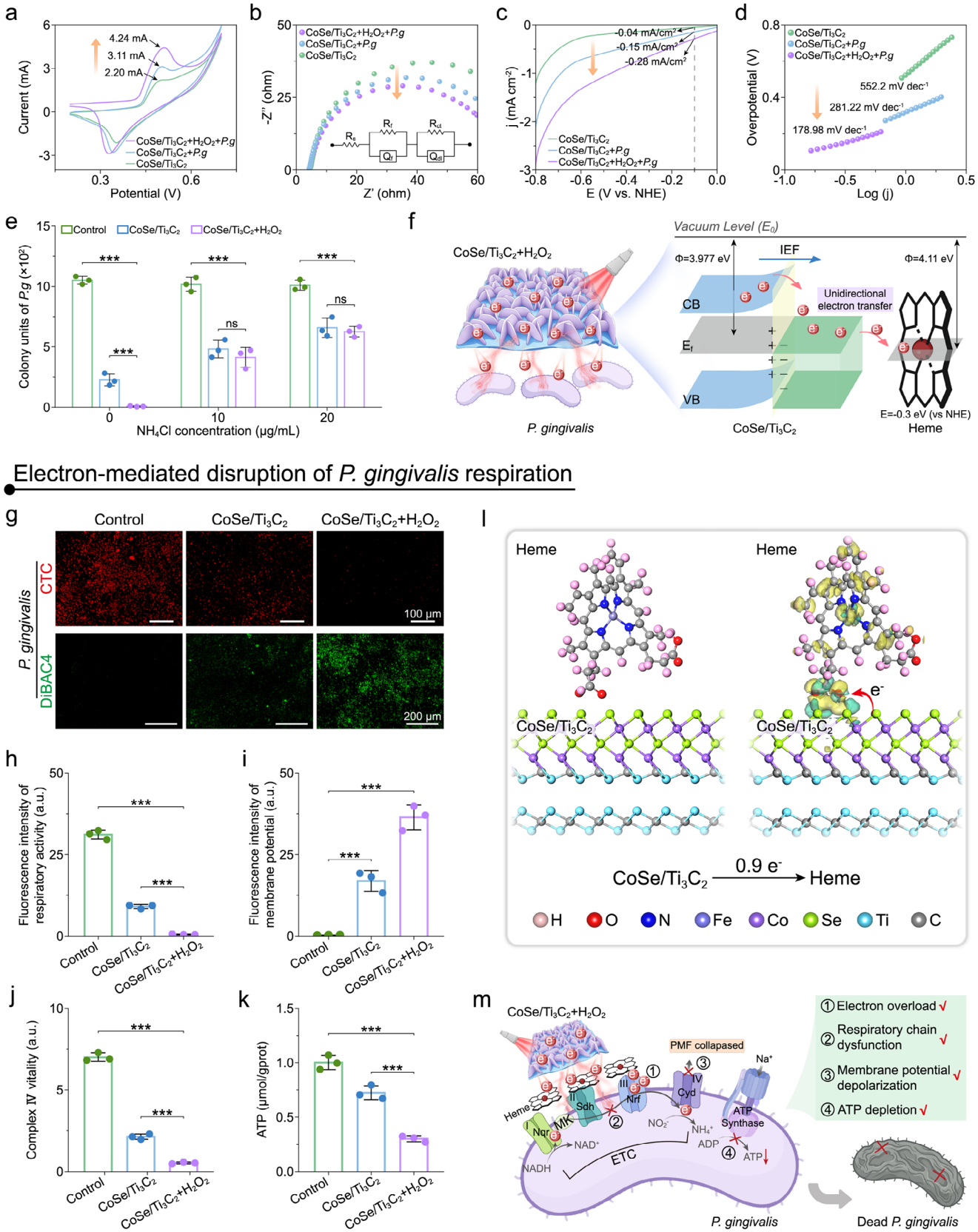


FIGURE 5 | Electron transfer from $CoSe/Ti_3C_2$ to bacteria under NIR. (a) CV curves, (b) Nyquist plots, (c) LSV curves, and (d) Tafel slopes of $CoSe/Ti_3C_2$, $CoSe/Ti_3C_2$+*P. gingivalis* and $CoSe/Ti_3C_2$+H_2O_2+*P. gingivalis* groups. (e) Colony-forming units of *P. gingivalis* under various concentrations of the electron-transfer blocker NH_4Cl ($n = 3$ independent replicates). (f) Schematic illustration of electron transfer from the $CoSe/Ti_3C_2$ to the heme

15214095, 0, Downloaded from https://advanced.onlinelibrary.wiley.com/doi/10.1002/adma.75394 by Sichuan University, Wiley Online Library on [23/10/2026]. See the Terms and Conditions (https://onlinelibrary.wiley.com/terms-and-conditions) on Wiley Online Library for rules of use; OA articles are governed by the applicable Creative Commons License

is further amplified under NIR irradiation, where the LSPR effect promotes a more vigorous electron flux.

Unlike most bacteria, *P. gingivalis* lacks porphyrin biosynthesis capabilities and strictly relies on the continuous acquisition of exogenous heme, which is abundantly immobilized on its outer membrane. This membrane-bound heme is not merely a critical nutrient; its highly conjugated iron-porphyrin architecture confers pronounced redox activity and electron transfer capacity, which may function as an electron reservoir and mediator [44, 45]. As illustrated in Figure 5f, the E_f of CoSe/Ti_3C_2 is determined to be −0.46 eV, which is markedly more negative compared to the redox potential of heme (−0.3 eV vs. NHE). This well-matched energy band structure establishes a thermodynamically favorable gradient, driving a targeted and unidirectional interfacial electron transfer from the CoSe/Ti_3C_2 heterojunction directly to the bacterial heme, thereby fatally short-circuiting its normal cellular respiration. To corroborate this mechanistic pathway, we modeled the electron transfer between heme and CoSe/Ti_3C_2 and further quantified it via Bader charge analysis, which reveals that the CoSe/Ti_3C_2 overloads electrons in the heme domains (Figure 5l).

Driven by the targeted interfacial electron transfer toward the membrane-bound heme, we hypothesize that the natural electron transport chain (ETC) of *P. gingivalis* would be fatally interrupted. To comprehensively validate this respiratory short-circuiting, the activities of the respiratory chain were evaluated using 2-para-(iodophenyl)-3-(nitrophenyl)-5-(phenyl) tetrazolium chloride (INT) and 5-cyano-2,3-ditolyl tetrazolium chloride (CTC) reduction assays. First, a quantitative analysis was conducted via the INT reduction assay, confirming that the CoSe/Ti_3C_2+H_2O_2 treatment leads to a significant 13.86% decline in overall dehydrogenase activity (Figure S50). Subsequently, to intuitively verify this metabolic suppression, a CTC fluorescent probe was introduced. CLSM images clearly reveal a dramatic quenching of the intracellular red fluorescence in the treated group, which highly aligns with the quantitative INT results (Figure 5g,h and Figure S51). Biologically, the structural and functional integrity of the ETC is a prerequisite for maintaining the proton motive force [44]. Consequently, the severe disruption of electron transport inevitably leads to the collapse of the transmembrane proton gradient. This is confirmed by the membrane potential assay, where the CoSe/Ti_3C_2+H_2O_2-treated bacteria exhibit a marked depolarization of the cellular membrane (Figure 5g,i and Figure S52). Moreover, changes in bacterial ETC complex activity across treatment groups were assessed using enzyme-linked immunosorbent assay (ELISA), showing that the activity of complex IV is significantly inhibited after co-incubation with CoSe/Ti_3C_2+H_2O_2 (Figure 5j). Simultaneously, based on the aforementioned disruption of the ETC by electron transfer, we hypothesize that ATP synthesis in bacteria would be severely impaired, leading to a sustained energy-starvation state. As expected, ATP levels of *P. gingivalis* in the CoSe/Ti_3C_2+H_2O_2 group exhibit the lowest ATP content, with bacterial viability almost completely abolished (Figure 5k). Based on these findings, Figure 5m summarizes the proposed antibacterial mechanism, in which interference with electron transfer disrupts bacterial energy metabolism. CoSe/Ti_3C_2+H_2O_2 with enhanced electron-donating ability exerts electron flow into crucial enzymes of the ETC via heme, leading to electron stacking, which disrupts the bacterial respiratory chain function. Thus, this disruption impairs the proton gradient required for ATP synthesis. It should be noted that the detailed respiratory mechanism described above was established primarily in *P. gingivalis*. Given the respiratory plasticity of *S. aureus* under different oxygen conditions, the specific ETC components affected by electron-transfer perturbation may differ between bacterial species.

2.5 | Antibacterial Mechanism Involving Interference With Electron Transfer Chain

Gene transcriptomic analysis was further conducted to gain insights into the comprehensive antibacterial mechanism of CoSe/Ti_3C_2 on *P. gingivalis*. Principal component analysis (PCA) of the transcriptomic profiles revealed clear segregation between the control and treatment groups in principal component space, highlighting substantial alterations in their transcriptomic profiles (Figure 6a). Correlation analysis confirms high intra-group consistency (Figure S53). Volcano plots reveal that the CoSe/Ti_3C_2+H_2O_2 group exhibits 934 significantly differentially expressed genes (DEGs) compared with the Control, with 862 genes downregulated and 72 genes upregulated (Figure 6b). Then, the DEGs are collected for hierarchical clustering analysis (Figure 6c). CoSe/Ti_3C_2+H_2O_2-treated *P. gingivalis* exhibits an evidently different gene expression pattern from the Control (untreated *P. gingivalis*). Gene ontology (GO) enrichment analysis shows that the downregulated DEGs are mainly enriched in gene expression, protein synthesis, and structural construction. The upregulated genes are mainly associated with disruption-induced stress, including unfolded protein binding and responses to chemical, stress, heat, and other abiotic stimuli (Figure S54). These transcriptional changes are consistent with ETC dysfunction and impaired bacterial metabolic and stress-response processes.

The DEGs are further subjected to Kyoto Encyclopedia of Genes and Genomes (KEGG) enrichment analysis to explore the biological pathways involved, showing that CoSe/Ti_3C_2+H_2O_2 significantly affects genes primarily enriched in propanoate metabolism, pyruvate metabolism, butanoate metabolism, nicotinate and nicotinamide metabolism, ubiquinone and

of *P. gingivalis*, created in BioRender. Chen, W. (2026) https://BioRender.com/5mlo8qx. (g) Bacterial CTC staining and membrane potential images of *P. gingivalis* cultured with various samples, and (h,i) corresponding fluorescence intensity statistics ($n = 3$ independent replicates). (j) The activity of the bacterial respiratory chain and (k) ATP levels after different treatments ($n = 3$ independent replicates). (l) Electron density difference plots at the heme and CoSe/Ti_3C_2 interface from the sideview. (m) Schematic diagram of the antibacterial mechanism involving the disruption of bacterial energy metabolism by interfering with electron transfer, created in BioRender. Chen, W. (2026) https://BioRender.com/5mlo8qx. All data are presented as mean ± SD. One-way ANOVA followed by Tukey's post hoc test was used. Significant differences between groups were indicated as $^{***}p < 0.001$, $^{**}p < 0.01$, $^{*}p < 0.05$, and ns represents not significant.

15214095, 0, Downloaded from https://advanced.onlinelibrary.wiley.com/doi/10.1002/adma.75394 by Sichuan University, Wiley Online Library on [23/10/2026]. See the Terms and Conditions (https://onlinelibrary.wiley.com/terms-and-conditions) on Wiley Online Library for rules of use; OA articles are governed by the applicable Creative Commons License

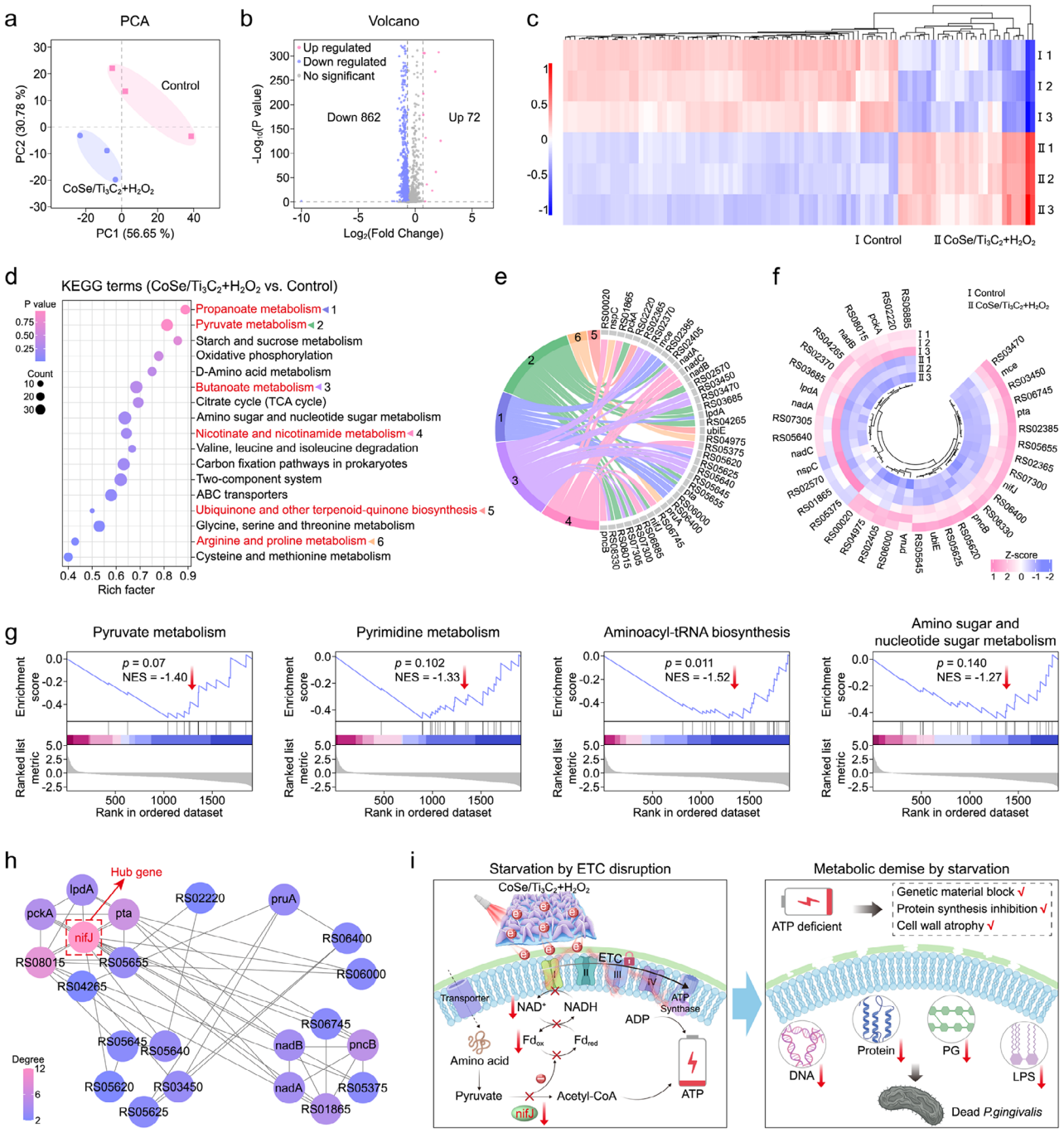


FIGURE 6 | Transcriptomic analysis of *P. gingivalis* under NIR. (a) PCA analysis and (b) Volcano plot of the DEGs for *P. gingivalis* after CoSe/Ti_3C_2 + H_2O_2 treatment compared with untreated Control. (c) Heatmap with hierarchical clustering of DEGs across replicate samples. (d) KEGG pathway enrichment analysis of the DEGs. (e) Chord plot linking representative DEGs to enriched pathways. (f) Circular heatmap showing expression changes in selected metabolism-related genes. (g) GSEA plots for representative metabolic pathways. (h) PPI network of the DEGs, with *nifJ* highlighted as a hub gene. (i) Schematic mechanism of treatment-induced electron transport chain dysfunction and metabolic demise in *P. gingivalis*, created in BioRender. Chen, W. (2026) https://BioRender.com/5mlo8qx. $n = 3$ independent replicates; all data are presented as mean ± SD. One-way ANOVA followed by Tukey's post hoc test was used. Significant differences between groups were indicated as $^{***}p < 0.001$, $^{**}p < 0.01$, $^{*}p < 0.05$, and ns represents not significant.

other terpenoid-quinone biosynthesis, and arginine and proline metabolism (Figure 6d), indicating that the bacterial energy metabolism is greatly affected. The chord diagram (Figure 6e) illustrates a detailed overview of representative genes involved in the aforementioned pathways, indicating a functionally interconnected metabolic network that disrupts the respiratory chain of *P. gingivalis*, thereby reprogramming its energy metabolism. The corresponding genes involved in these pathways are significantly downregulated (Figure 6f). Protein–protein interaction (PPI) network analysis of these DEGs reveals functional interconnectivity among metabolic genes, highlighting critical points of energy metabolic disruption

15214095, 0, Downloaded from https://advanced.onlinelibrary.wiley.com/doi/10.1002/adma.75394 by Sichuan University, Wiley Online Library on [23/10/2026]. See the Terms and Conditions (https://onlinelibrary.wiley.com/terms-and-conditions) on Wiley Online Library for rules of use; OA articles are governed by the applicable Creative Commons License

under electron transfer (Figure 6h). This discovery highlights the potential role of pyruvate: ferredoxin (flavodoxin) oxidoreductase (*nifJ*) in the energy metabolism of *P. gingivalis*, providing important clues for understanding its potential role in biological processes.

As an obligate anaerobe, *P. gingivalis* generates pyruvate mainly from amino acid catabolism, which is then processed through pyruvate and butanoate metabolism to yield ATP via substrate-level phosphorylation [46]. In-depth analysis of bacterial metabolic alterations using GSEA reveals a downregulation of pathways associated with energy production and biosynthesis (Figure 6g and Figure S55). Although glycolysis contributes limited ATP, it supplies essential intermediates such as pyruvate and NADH; thereby, the downregulation of pyruvate, butanoate, and glycolysis/gluconeogenesis pathways indicates impaired energy metabolism and reduced ATP production [47]. On the other hand, nucleotide biosynthesis via pyrimidine and purine pathways, along with protein synthesis and cell wall/LPS construction mediated by ribosome and amino sugar/nucleotide sugar metabolism, are highly energy-consuming, and their downregulation likely reflects an adaptive response of bacteria to energy-limited or stressful conditions, conserving energy and promoting survival under starvation or other adverse environments [48, 49]. Based on these comprehensive experimental data, we propose a refined mechanism of metabolic demise induced by bio-interfacial electron stacking, as illustrated in Figure 6i. Specifically, CoSe/Ti_3C_2-mediated electron transfer disrupts the ETC and *nifJ*-dependent pyruvate metabolism, resulting in impaired redox cycling and ATP depletion. The resulting energy deficiency suppresses the biosynthesis of DNA, proteins, peptidoglycan, and LPS, ultimately leading to the structural disintegration and death of *P. gingivalis*.

2.6 | Bone Homeostasis Restoration Through Promotion of Osteogenesis

Having validated the integrated antibacterial and antioxidase-mimetic functions of ERR-HJ, we next evaluated its osteoinductive potential in human periodontal ligament cells (hPDLCs), key regulators of periodontal bone regeneration. Biocompatibility was first validated by CCK-8 assays, which showed minimal cytotoxicity against hPDLCs at concentrations of 0∼5 μg/mL (Figure S56a–d), while SEM and Live/Dead staining confirmed well-spread cells with intact morphology (Figure S56e,f). Phalloidin staining reveals that hPDLCs cultured with various samples for 24 h retain spindle or polygonal shapes, maintain intact cytoskeletal structures, and exhibit prominent protrusions without disruption (Figure S57a). Scratch assays demonstrate that ERR-HJ enhances hPDLC migration (Figure S57b), with cells cultured in the presence of Ti_3C_2-containing composites showing greater migratory potential compared to those cultured with CoSe alone (Figure S57c), consistent with previously reported MXene-associated pro-migratory effects [34].

To evaluate the osteogenic potential, hPDLCs were subjected to osteogenic induction (Osteo). Compared with the Osteo and CoSe groups, both CoSe/Ti_3C_2 and ERR-HJ-treated hPDLCs cultured in osteogenic induction medium (OIM) display markedly elevated alkaline phosphatase (ALP) activity, an early osteogenic marker, and increased mineralized nodule formation as indicated by Alizarin Red S (ARS) staining, a late-stage osteogenic marker (Figure 7a) [19]. Quantitative ALP assays reveal that CoSe/Ti_3C_2 and ERR-HJ groups exhibit significantly higher ALP activity than the Control (Figure 7b,c), while CoSe treatment alone still induces an upward trend in ALP levels at days 3 and 7, though without statistical significance. Quantification of matrix mineralization confirms that OIM efficiently induces osteogenic differentiation of hPDLCs, with CoSe, CoSe/Ti_3C_2, or ERR-HJ treatment all showing time-dependent promotion of mineralization (Figure 7d,e).

Se, an essential trace element incorporated into selenoproteins, contributes to bone homeostasis by exerting antioxidant effects and regulating osteoblast and osteoclast activity [50, 51]. Among selenoproteins, Glutathione peroxidase 1 (GPX1) is a key regulator of redox balance in skeletal progenitors and has been reported to promote osteogenic differentiation and matrix mineralization, while selenophosphate synthetases (SEPHS1/2) are essential enzymes driving intracellular Se metabolism and selenoprotein biosynthesis [27, 50, 52, 53]. Given the osteoinductive potential of Se-incorporated heterojunction, we speculate that this effect might be associated with Se metabolism. To further confirm this hypothesis, RT-qPCR analysis was performed. Upregulated expression of early osteogenic genes, including runt-related transcription factor 2 (*RUNX2)* and *ALPL*, selenoproteins (*GPX1*, *SEPHS2*), as well as the late-stage osteogenic marker osteopontin (*OPN*), is observed in CoSe, CoSe/Ti_3C_2, and ERR-HJ treatment groups, among which the CoSe treatment exhibits the strongest induction of *GPX1* and *SEPHS2*, suggesting a selenium-mediated regulatory role in osteogenesis (Figure 7f and Figure S58). Consistently, Western blotting confirms enhanced protein levels of collagen type I alpha 1 (COL1A1), RUNX2, and OPN, together with elevated selenoprotein (GPX1, SEPHS1, and SEPHS2) expression in the CoSe/Ti_3C_2 and ERR-HJ groups (Figure 7g). Immunofluorescence staining reveals stronger COL1A1 and RUNX2 signals in the CoSe, CoSe/Ti_3C_2, and ERR-HJ groups (Figure 7i,j), and semiquantitative analysis demonstrates that ERR-HJ significantly enhances RUNX2 transcriptional activity and COL1A1 secretion in hPDLCs compared to the Control (Figure 7k,l). These results collectively demonstrate that ERR-HJ enhances osteogenesis and selenoprotein expression in hPDLCs (Figure 7h). This pro-osteogenic modulation of hPDLCs by ERR-HJ constitutes a substantial contributor to periodontal tissue restoration and disease remission.

2.7 | GPX1/GSH-Coordinated Redox Defense Strengthening and Macrophage Phenotypic Switching-Mediated Osteoimmunological Reprogramming

Inspired by the ROS-scavenging capacity of CoSe/Ti_3C_2 and ERR-HJ, we evaluated their ability to mitigate oxidative stress under inflammatory conditions using macrophage-lineage cells, which serve as osteoclast precursors and play central roles in orchestrating osteoimmune regulation during bone remodeling [54–56]. ERR-HJ and individual components display excellent cytocompatibility at 0∼5 μg/mL with murine macrophage cell

15214095, 0, Downloaded from https://advanced.onlinelibrary.wiley.com/doi/10.1002/adma.75394 by Sichuan University, Wiley Online Library on [23/10/2026]. See the Terms and Conditions (https://onlinelibrary.wiley.com/terms-and-conditions) on Wiley Online Library for rules of use; OA articles are governed by the applicable Creative Commons License

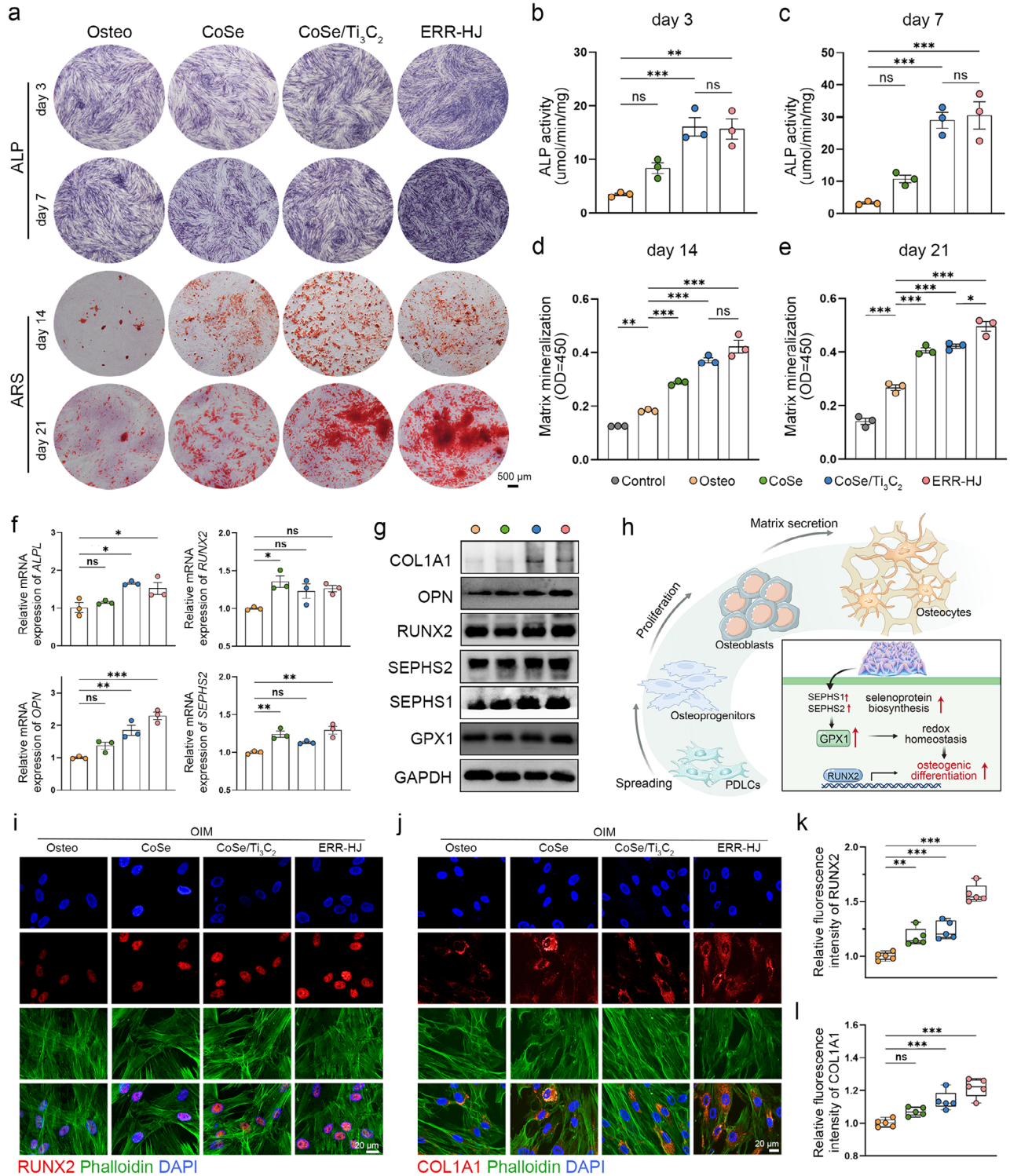


FIGURE 7 | In vitro osteogenic differentiation in hPDLCs. (a) ALP staining (days 3 and 7) and ARS staining (days 14 and 21) of hPDLCs. (b,c) Quantitative analysis of ALP activity on days 3 and 7 ($n = 3$ independent replicates). (d,e) Quantification of matrix mineralization on days 14 and 21. (f) RT-qPCR analysis of relative mRNA expression of early osteogenic marker genes (*ALPL*, *RUNX2*), selenoprotein-related genes (*GPX1*, *SEPHS2*) at day 3, and the late-stage osteogenic marker *OPN* at day 14. (g) Western blot analysis of osteogenic-related proteins (COL1A1, OPN, and RUNX2) and selenoproteins (SEPHS1, SEPHS2, and GPX1) in hPDLCs treated with different groups ($n = 3$ independent replicates). (h) Schematic diagram illustrating that ERR-HJ enhances selenoprotein biosynthesis to restore redox homeostasis and promote osteogenic differentiation of hPDLCs, thereby boosting osteogenesis, created in BioRender. Chen, W. (2026) https://BioRender.com/5mlo8qx. (i) Immunofluorescence images of RUNX2 and FITC-phalloidin in hPDLCs. (j) Immunofluorescence images of COL1A1 and FITC-phalloidin in the hPDLCs ($n = 4$ independent replicates). (k,l) Semiquantification of relative fluorescence intensity of RUNX2 and COL1A1 in (i) and (j). All data are presented as mean ± SE. One-way ANOVA followed by Tukey's post hoc test was used. Significant differences between groups were indicated as ***$p < 0.001$, **$p < 0.01$, *$p < 0.05$, and ns represents not significant.

15214095, 0, Downloaded from https://advanced.onlinelibrary.wiley.com/doi/10.1002/adma.75394 by Sichuan University, Wiley Online Library on [23/10/2026]. See the Terms and Conditions (https://onlinelibrary.wiley.com/terms-and-conditions) on Wiley Online Library for rules of use; OA articles are governed by the applicable Creative Commons License

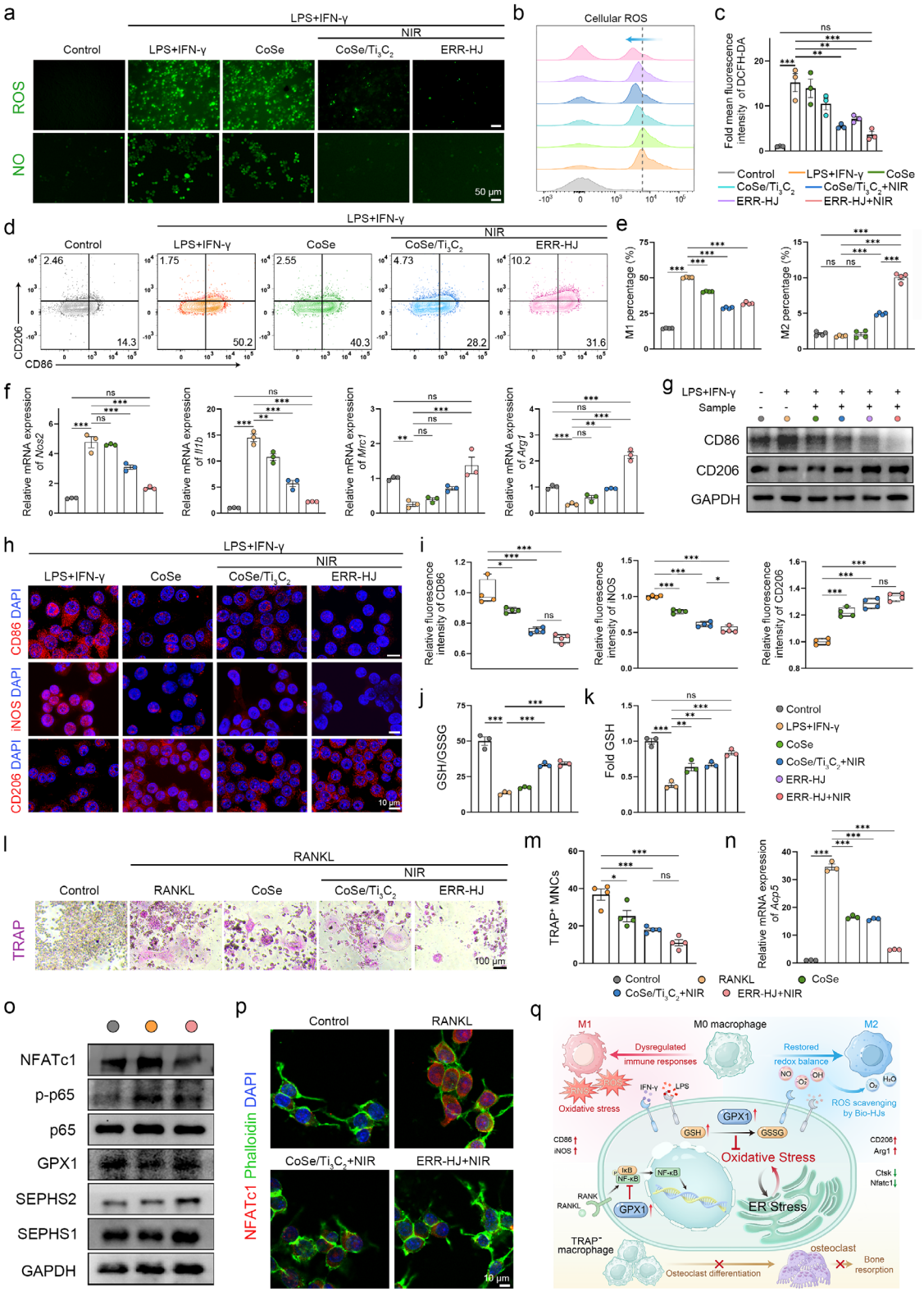


FIGURE 8 | Selenoprotein-mediated redox regulation, coupled with ROS elimination, promotes macrophage anti-inflammatory polarization. (a) Intracellular ROS levels (upper panels, detected using DCFH-DA) and NO (lower panels, detected using DAF-FM DA) levels in RAW 264.7 cells (n = 3 independent replicates). (b) Flow cytometry analysis of intracellular ROS detected by DCFH-DA. (c) Quantification of fold mean fluorescence intensity measured by flow cytometry (n = 3 independent replicates). (d) Representative flow cytometry plots showing macrophage polarization (n = 4 independent replicates), with $CD86^+/CD206^-$ as M1-like phenotype and $CD206^+/CD86^-$ as M2-like phenotype. (e) Quantitative analysis of M1 and M2 macrophage percentages. (f) Relative mRNA expression levels of M1 markers (*Nos2* and *Il1b*) and M2 markers (*Mrc1* and *Arg1*) in RAW 264.7 cells, determined by RT-qPCR (n = 3 independent replicates). (g) Western blot analysis of CD86 and CD206 (n = 3 independent replicates). (h) Immunofluorescence images of CD86, iNOS, and CD206 in RAW 264.7 cells (n = 4 independent replicates). (i) Semiquantification of relative fluorescence

15214095, 0, Downloaded from https://advanced.onlinelibrary.wiley.com/doi/10.1002/adma.75394 by Sichuan University, Wiley Online Library on [23/10/2026]. See the Terms and Conditions (https://onlinelibrary.wiley.com/terms-and-conditions) on Wiley Online Library for rules of use; OA articles are governed by the applicable Creative Commons License

line RAW 264.7, as evidenced by cell viability, SEM and Live/Dead staining (Figure S59). The concentration of 5 μg/mL was selected for the in vitro experiments and an inflammatory model of RAW 264.7 cells was established by treatment with LPS from *P. gingivalis* (Pg-LPS) and Interferon-γ (IFN-γ) as previously reported [20]. Intracellular oxidative stress in macrophages was quantified using DAF-FM DA for NO and DCFH-DA for ROS, revealing strong green fluorescence in Pg-LPS+IFN-γ-treated and CoSe-treated cells, whereas untreated cells show minimal signals, indicating high levels of ROS and NO induced by inflammation (Figure 8a). ERR-HJ treatment, particularly under NIR, markedly reduces ROS and NO levels in macrophages, while CoSe, CoSe/Ti_3C_2, and ERR-HJ without NIR also decrease these levels, albeit less effectively. Flow cytometry analysis reveals a rightward shift in fluorescence peaks for Pg-LPS+IFN-γ versus the Control group, which is mitigated by CoSe, CoSe/Ti_3C_2, or ERR-HJ treatments, with NIR further enhancing scavenging efficiency (Figure 8b and Figure S60a). Additionally, quantitative analysis corroborates these findings, showing that ERR-HJ with NIR restores ROS and NO levels close to baseline (Figure 8c and Figure S60b). To assess the effects of ERR-HJ on endogenous antioxidant defenses, reduced glutathione (GSH) content and the GSH/oxidized glutathione (GSSG) ratio were quantified [57]. Inflammatory stimulation leads to a significant reduction in the GSH/GSSG ratio, whereas CoSe, CoSe/Ti_3C_2, and ERR-HJ treatments significantly restore the ratio, with NIR providing enhanced restoration, bringing the ratio almost to physiological levels (Figure 8j). Similarly, total GSH levels are largely restored by ERR-HJ under NIR (Figure 8k).

Macrophages display notable plasticity, swiftly adapting their phenotypes to sustain homeostasis, clear debris, and facilitate tissue repair [37, 58]. By labeling M1 ($CD86^+/CD206^-$) and M2 ($CD206^+/CD86^-$) markers, flow cytometry reveals that Pg-LPS+IFN-γ induces pronounced M1 polarization (Figure 8d,e). In contrast, treatment with CoSe/Ti_3C_2 and ERR-HJ under NIR markedly suppresses the proportion of M1 macrophages while promoting the emergence of M2 macrophages. RT-qPCR analysis reveals elevated mRNA levels of nitric oxide synthase 2 (*Nos2*), interleukin-6 (*Il6*), tumor necrosis factor (*Tnf*), and interleukin-1β (*Il1b*) (M1 markers), along with decreased levels of arginase 1 (*Arg1*) and mannose receptor C-type 1 (*Mrc1*, also known as CD206) (M2 markers) in the Pg-LPS+IFN-γ group, both of which are markedly reversed by CoSe/Ti_3C_2 and ERR-HJ treatment (Figure 8f and Figure S61). Western blotting confirms this trend, showing a significant decrease in expression of CD86, with increased CD206 expression in ERR-HJ-treated macrophages (Figure 8g). Additional analysis of inducible nitric oxide synthase (iNOS) and C—C motif chemokine receptor 7 (CCR7), two M1-associated markers, showed increased expression following LPS+IFN-γ stimulation and reduced expression after ERR-HJ treatment, with the greatest reduction observed in the ERR-HJ+NIR group (Figure S62). Immunofluorescence for CD86, iNOS, and CD206 corroborates these findings, suggesting that ERR-HJ significantly shifts macrophage polarization toward the anti-inflammatory M2 state (Figure 8h,i).

Osteoclasts are multinucleated bone-resorbing cells derived from the monocyte–macrophage lineage, representing another important differentiation fate of macrophage-lineage cells [55]. Emerging evidence indicates that selenoproteins modulate osteoclastogenesis and bone resorption via regulation of intracellular redox balance and nuclear factor κB (NF-κB)-dependent signaling, thereby contributing to bone homeostasis [56, 59]. Based on this, we hypothesize that ERR-HJ may affect osteoclast differentiation. TRAP staining revealed markedly fewer multinucleated osteoclasts following ERR-HJ treatment in RANKL-stimulated RAW 264.7 cells, indicating suppressed osteoclast formation (Figure 8l,m). RT-qPCR analysis shows downregulation of osteoclast-related genes, including Acid phosphatase 5 (*Acp5*), Matrix metalloproteinase 9 (*Mmp9*), Cathepsin K (*Ctsk*), and Nuclear factor of activated T cells 1 (*Nfatc1*), and concurrent upregulation of the selenoprotein *Gpx1* (Figure 8n and Figure S63) [56]. NF-κB signaling constitutes a principal transduction pathway in osteoclast differentiation and its role in osteoclastogenesis was further examined by Western blotting of P65 phosphorylation levels. The results demonstrate that CoSe/Ti_3C_2 and ERR-HJ inhibit NFATc1 expression, suppress P65 phosphorylation and upregulate selenoprotein expression, indicating blocked osteoclast differentiation accompanied by activation of Se metabolism (Figure 8o). Fluorescence staining of NFATc1 further validates these results, showing strong induction by RANKL but reversed by ERR-HJ treatment (Figure 8p). The illustrative scheme of osteoimmunological reprogramming mediated by macrophage phenotypic switching is presented in Figure 8q.

2.8 | Therapeutic Efficacy in a Periodontitis Animal Model Through Anti-Inflammatory Modulation, Osteoclastogenesis Suppression, and Oxidative Stress Amelioration

Given the ability of ERR-HJ to simultaneously enhance osteogenesis and restore redox-driven osteoimmune balance in vitro, we proceeded to assess its therapeutic performance in a ligature-induced periodontitis (LIP) rat model (Figure 9a,b). After 2 weeks of treatment, the ligatures were removed and maxillary bone and blood were harvested for examinations. To directly visualize alveolar bone changes, micro-CT scanning with three-dimensional

intensity of CD86, iNOS and CD206 in (h). (j) Intracellular glutathione redox status assessed by the GSH/GSSG ratio and (k) Fold GSH ($n = 3$ independent replicates). (l) TRAP staining of RANKL-stimulated RAW 264.7 cells. (m) Quantification of TRAP-positive multinucleated cells (≥ 3 nuclei). (n) Relative mRNA expression of *Acp5* determined by RT-qPCR ($n = 3$ independent replicates). (o) Western blot analysis of osteoclast-related proteins (NFATc1, phosphorylated p65, and p65) and selenoproteins (GPX1, SEPHS1, and SEPHS2) in RAW 264.7 cells. (p) Immunofluorescence images of NFATc1 and FITC-phalloidin. (q) Schematic illustration of the mechanisms of ERR-HJ-mediated osteoimmunological reprogramming by macrophage phenotypic switching, created in BioRender. Chen, W. (2026) https://BioRender.com/5mlo8qx. All data are presented as mean ± SE. One-way ANOVA followed by Tukey's post hoc test was used. Significant differences between groups were indicated as ***$p < 0.001$, **$p < 0.01$, *$p < 0.05$, and ns represents not significant.

15214095, 0, Downloaded from https://advanced.onlinelibrary.wiley.com/doi/10.1002/adma.75394 by Sichuan University, Wiley Online Library on [23/10/2026]. See the Terms and Conditions (https://onlinelibrary.wiley.com/terms-and-conditions) on Wiley Online Library for rules of use; OA articles are governed by the applicable Creative Commons License

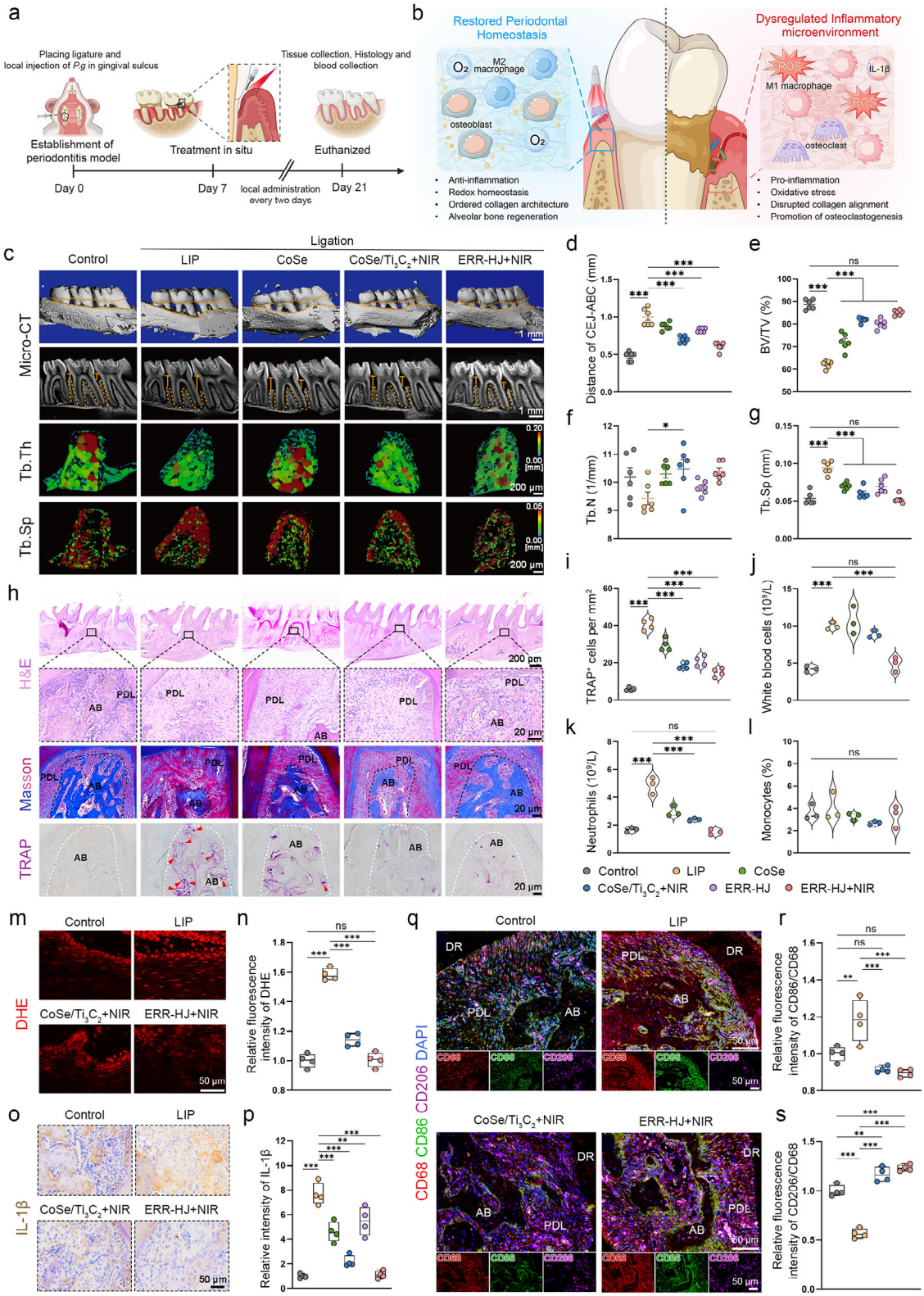


FIGURE 9 | Attenuating periodontitis progression by mitigating pro-inflammatory damage, alleviating oxidative stress and reducing alveolar bone loss. (a) Experimental scheme for construction of the LIP periodontitis rat model, created in BioRender. Chen, W. (2026) https://BioRender.com/w84m1rj. (b) Schematic illustration of ERR-HJ-mediated ROS-scavenging, anti-inflammatory reprogramming, and osteoclast suppression that synergistically contribute to alveolar bone protection, created in BioRender. Chen, W. (2026) https://BioRender.com/w84m1rj. (c) Representative 3D reconstructions (top panels) and sagittal-plane micro-CT images (second panels) of the maxillary alveolar bone ($n = 6$ independent replicates). The yellow dashed line outlines alveolar cortical bone, and the yellow segments indicate CEJ-ABC distance. Trabecular thickness (Tb.Th) and Tb.Sp at the root furcation of the second Molar are shown below. (d) Quantification of the CEJ-ABC distances at the sites mesial or distal to the second Molar ($n = 6$ independent replicates). (e–g) Quantification of BV/TV, Tb.Sp and Tb.N at the furcation of the second Molar ($n = 6$ independent replicates). (h) H&E staining for overall

15214095, 0, Downloaded from https://advanced.onlinelibrary.wiley.com/doi/10.1002/adma.75394 by Sichuan University, Wiley Online Library on [23/10/2026]. See the Terms and Conditions (https://onlinelibrary.wiley.com/terms-and-conditions) on Wiley Online Library for rules of use; OA articles are governed by the applicable Creative Commons License

reconstruction was performed, with linear cemento-enamel junction (CEJ) to the alveolar bone crest (ABC) distances at the second molar (second Molar) used as an index of bone resorption (Figure 9c and Figure S64a). The LIP group displays pronounced bone destruction surrounding the second Molar, while treatment with CoSe/Ti_3C_2 and ERR-HJ under 808 nm NIR achieves remarkable recovery of bone height and morphology. NIR illumination potentiates the bone regenerative efficacy of both CoSe/Ti_3C_2 and ERR-HJ treatments, underscoring the pivotal role of photoactivated antibacterial activity in mitigating bone resorption (Figure 9d). In vivo thermal imaging under the therapeutic irradiation conditions (808 nm, 1.5 W cm^{-2}, 5 min) shows comparable temperatures in the PBS+NIR and ERR-HJ+NIR groups after 5 min (Figure S65). Although a minor contribution from mild local heating cannot be excluded, no appreciable ERR-HJ-induced additional heating is observed [60, 61]. Quantitative morphometric analysis at the root bifurcation of the second Molar reveals that all Se-incorporated groups demonstrate improved bone volume/total volume (BV/TV) ratio compared with the LIP group, with ERR-HJ+NIR restoring BV/TV to levels comparable to the Control group, implicating taurine as a contributor to bone protection (Figure 9e). Similar improvements are observed in trabecular number (Tb.N), whereas trabecular separation (Tb.Sp) is markedly reduced after treatment compared with the LIP group, confirming the bone-restoring efficacy of CoSe/Ti_3C_2 and ERR-HJ (Figure 9f,g).

Histological evaluations by hematoxylin and eosin (H&E) staining, Masson's trichrome staining and tartrate-resistant acid phosphatase (TRAP) staining reveal extensive inflammatory infiltration and periodontal fiber destruction in the LIP group, while ERR-HJ+NIR treatment markedly ameliorates these lesions, restoring ridge height and periodontal fiber integrity (Figure 9h and Figure S64b). TRAP staining reveals multiple clusters of $TRAP^+$ osteoclasts in the LIP group but only sparse $TRAP^+$ cells in the ERR-HJ+NIR-treated group (Figure 9h and Figure S64b). Quantitative osteoclast analysis substantiates the morphological observations, confirming the pronounced inhibition of osteoclastogenesis by the Se-incorporated heterojunction (Figure 9i), consistent with in vitro observations. It has been previously reported that periodontitis is correlated with elevated leukocyte and neutrophil counts in hematological profiles, indicative of an increased systemic inflammatory burden [62]. Accordingly, we evaluated immune cell profiles in peripheral blood. The LIP group induces elevated leukocyte and neutrophil counts, which are normalized after ERR-HJ+NIR treatment, whereas monocyte levels remain unaffected across all groups (Figure 9j–l).

Considering the restored periodontal tissue integrity and the oxidative stress-regulating efficacy of CoSe/Ti_3C_2 and ERR-HJ observed in vitro, we propose that CoSe/Ti_3C_2 and ERR-HJ may act as effective ROS scavengers in vivo within inflammatory microenvironments. The LIP model induces enhanced ROS signals shown by dihydroethidium (DHE) staining in the periodontal tissue, while ERR-HJ+NIR treatment abrogates this effect, providing direct evidence of ROS scavenging in vivo (Figure 9m,n). Immunohistochemical (IHC) staining revealed reduced RUNX2 and COL1A1 expression in the LIP group compared with the Control group, whereas ERR-HJ treatment restored both markers, with the most pronounced staining observed in the ERR-HJ+NIR group (Figure S66). In addition, IL-1β expression is significantly elevated in the LIP group but restored to baseline after ERR-HJ+NIR treatment (Figure 9o,p and Figure S67). These findings further support the enhanced periodontal bone regeneration observed by micro-CT. Macrophage polarization critically governs the trajectory of periodontitis, with M1 macrophages amplifying inflammatory responses and M2 macrophages promoting resolution and tissue regeneration [6, 54]. Immunofluorescence analysis shows predominant $CD68^+/CD86^+$ M1 macrophage infiltration and diminished $CD206^+$ M2 phenotype in the LIP group (Figure 9q,r). Notably, ERR-HJ+NIR treatment promotes a robust shift toward the reparative M2 phenotype, as evidenced by a substantial increase in the $CD206^+/CD68^+$ cell ratio. This shift, consistent with our in vitro findings, underscores its potent immunomodulatory capacity to resolve periodontal inflammation (Figure 9q,s). Collectively, these findings establish ERR-HJ as a multifunctional platform that synergistically restores alveolar bone homeostasis, suppresses inflammation, scavenges ROS, and orchestrates osteoimmune balance. No noticeable abnormalities are observed in histopathology of major organs and hematological profiles, supporting the biosafety of ERR-HJ for local administration (Figures S68 and S69). Body weight was monitored throughout the treatment period to assess general physiological status, and no significant differences were observed among the groups over the 21-day experimental period (Figure S70). Since the ligature-induced model does not fully recapitulate the chronic progression of human periodontitis, the therapeutic potential of ERR-HJ in chronic periodontal conditions warrants further validation in long-term polymicrobial and large-animal models. Moreover, developing novel delivery systems, such as mucoadhesive gels with high retention efficacy that resist salivary dilution, holds considerable promise for reconciling the need for non-invasive administration with the imperatives of reduced administration frequency and minimized off-target toxicity, representing a critical and worthwhile direction for future investigation.

observation (top panels) and enlarged views of the black-boxed regions (second panels) ($n = 4$ independent replicates). Masson's trichrome staining and TRAP staining are shown below, with red arrows indicating TRAP-positive cells. (i) Osteoclast counts based on TRAP staining. (j) Absolute counts of white blood cells and (k) neutrophils ($n = 3$ independent replicates). (l) Frequency of monocytes ($n = 3$ independent replicates). (m) DHE fluorescence staining revealing ROS levels in periodontal tissue and (n) semiquantification of relative fluorescence intensity ($n = 4$ independent replicates). (o) Immunohistochemical staining of IL-1β in the furcation region of the second Molar. (p) Semiquantification of the relative integrated optical density (IOD) of IL-1β in (o). (q) Representative images of multiplex immunofluorescence staining of macrophage polarization markers, including CD68, CD86, and CD206. (r) Relative fluorescence intensity ratios of CD86/CD68 and (s) CD206/CD68. PDL, periodontal ligament; DR, dental root; AB, alveolar bone. All data are presented as mean ± SE. One-way ANOVA followed by Tukey's post hoc test was used. Significant differences between groups were indicated as $^{***}p < 0.001$, $^{**}p < 0.01$, $^{*}p < 0.05$, and ns represents not significant.

15214095, 0, Downloaded from https://advanced.onlinelibrary.wiley.com/doi/10.1002/adma.75394 by Sichuan University, Wiley Online Library on [23/10/2026]. See the Terms and Conditions (https://onlinelibrary.wiley.com/terms-and-conditions) on Wiley Online Library for rules of use; OA articles are governed by the applicable Creative Commons License

2.9 | Mitigating Periodontitis Progression by Restoring Redox Homeostasis and Alleviating ER Stress via GPX1-PERK-CHOP Axis

Bulk transcriptomics combined with ssGSEA identifies ER stress activation and its association with inflammatory immune niches in periodontitis (Figure S1). We further performed whole-transcriptome RNA sequencing (RNA-seq) on periodontitis-affected gingival tissues in the LIP periodontitis model. PCA shows three distinct clusters corresponding to the experimental groups, with minimal overlap in the principal component space, indicating significant inter-group heterogeneity (Figure S71a). DEGs are scrutinized and shown in the volcano plot (Figure S71b,c). Hierarchical clustering of top DEGs shows distinct grouping, with the ERR-HJ group exhibiting a unique transcriptomic profile compared to the LIP group, indicating modulation of periodontitis-associated transcriptomic alterations (Figure S71d). GO and KEGG enrichment analyses were subsequently conducted to characterize the biological functions and pathways represented by the DEGs. Periodontitis-induced genes showed prominent enrichment in terms associated with inflammatory response, extracellular matrix remodeling, response to bacterium and oxidative stress (Figure S72). In addition to the pathways mentioned above, ERR-HJ treatment induces a marked transcriptomic profile shift characterized by DEGs enriched in oxidative stress response, glutathione metabolic process and unfolded protein binding, and protein processing in the endoplasmic reticulum (Figure 10a–c). The chord diagram further illustrates representative genes associated with the GO-enriched terms described above (Figure 10c), indicating the impact of ERR-HJ on oxidative homeostasis and ER stress. As shown in Figure 10d, GSEA shows enrichment of pathways related to inflammatory response and downregulation of extracellular matrix-associated pathways in the LIP model versus the healthy Control, consistent with the histological observations. Beyond suppressing inflammatory pathways, the ERR-HJ treatment significantly modulates the oxidation-reduction processes in the LIP model (Figure 10e), an effect aligning with the in vitro findings of its anti-inflammatory and ROS-scavenging capacity.

Building on the in vivo RNA-seq data, we next delineated the molecular mechanisms underlying ER stress regulation in RAW 264.7 cells. Ultrastructural evaluation of ER morphology by TEM reveals that inflammatory stimulation causes pronounced dilation of rough ER lumens, luminal flocculent material, and increased ER-mitochondrial contacts in macrophages. In contrast, ERR-HJ treatment markedly restores ER morphology to evenly widened, flattened tubular structures that are comparable to the Control group (Figure 10f). Upon oxidative stress, the luminal chaperone GRP78 dissociates from Inositol-requiring enzyme 1α (IRE1α), PERK, and Activating transcription factor 6 (ATF6) to relieve their inhibition and trigger UPR, a conserved adaptive signaling network activated by ER stress [9, 13]. RT-qPCR results demonstrate that Pg-LPS+IFN-γ stimulation induces robust upregulation of ER stress-related genes including *Hspa5* (GRP78), *Eif2ak3* (PERK), *Ern1* (IRE1α), and *Atf6*, as well as the downstream pro-apoptotic factor *Ddit3* (CHOP), indicating excessive ER stress activation and pro-apoptotic signaling (Figure S73). Treatment with CoSe/Ti_3C_2 and ERR-HJ partially reverses these changes, even in the absence of NIR irradiation, suggesting protection against inflammation-induced ER stress activation. Taurine cooperates with the heterojunction to mitigate ER stress-driven apoptotic signaling.

Considering the ability of the Se-incorporated heterojunction to modulate ER stress, we speculate that this might be associated with Se metabolism [63, 64]. Therefore, we evaluated the derivatives of Se in RAW 264.7 cells after 12 h of treatment by high-performance liquid chromatography coupled to inductively coupled plasma-mass spectrometry (HPLC-ICP-MS) assay, detecting SeO_3^{2-}(Se^{4+}), SeO_42^- (Se^{6+}), selenocystine ($SeCys_2$), methylselenocystine (MetSeCys) and SeMet. As shown in Figure 10g, ERR-HJ treatment under NIR irradiation significantly increases intracellular $SeCys_2$ relative to the Control group, indicating enhanced seleno-amino acid synthesis. Interestingly, Pg-LPS+IFN-γ stimulation leads to a significant depletion in $SeCys_2$, while Se-containing heterojunction treatment under inflammation partially restores the reduction, though not fully to control levels. Meanwhile, MetSeCys and SeMet are barely detected, possibly due to transient early upregulation and subsequent conversion into $SeCys_2$ for selenoprotein biosynthesis [50, 53, 65].

Although PERK, IRE1α, and ATF6 collectively coordinate the UPR, we focus subsequent mechanistic analyses on PERK-CHOP signaling as it was previously implicated in macrophage inflammatory activation and osteoclast differentiation [14, 66]. To clarify the involvement of selenoproteins in ERR-HJ-mediated oxidative and ER stress regulation, we quantified selenoprotein expression and the activation state of the GRP78-PERK-CHOP pathway. Western blotting demonstrates that both CoSe/Ti_3C_2 and ERR-HJ upregulate SEPHS1 and SEPHS2 while concomitantly suppressing GRP78 expression, PERK phosphorylation and CHOP activation, together with increased expression of the selenoprotein GPX1 (Figure 10k), a pivotal antioxidant enzyme involved in mitigating oxidative stress and maintaining ER homeostasis [50, 67]. Immunofluorescence of GRP78, p-PERK, GPX1 and CHOP in RAW 264.7 cells under different treatments confirms this expression pattern, further supporting an association between GPX1-centered redox regulation and attenuation of PERK-CHOP signaling during CoSe/Ti_3C_2- and ERR-HJ-mediated ER stress alleviation (Figure 10i,j and Figure S74). To further evaluate the involvement of the PERK-CHOP pathway in ERR-HJ-mediated ER stress regulation, we performed pharmacological activation of PERK using CCT020312 [68]. CCT020312 increases PERK phosphorylation and CHOP expression and partially attenuates the inhibitory effects of ERR-HJ on the PERK-CHOP axis (Figure S75a), supporting the involvement of PERK-CHOP signaling in ERR-HJ-mediated ER stress regulation. We then examined the effects of ERR-HJ on PERK-CHOP signaling in the absence of inflammatory stimulation. Even without LPS+IFN-γ stimulation, the CCT020312-induced elevation of PERK phosphorylation and CHOP expression is attenuated by ERR-HJ+NIR treatment in macrophages (Figure S75b). Notably, the elevated GPX1 expression induced by ERR-HJ+NIR is maintained in the presence of CCT020312. Together, these results further support the involvement of GPX1 in ERR-HJ-mediated suppression of PERK-CHOP signaling. The periodontal ligament in the LIP group exhibits reduced GPX1 and elevated GRP78 expression, both of which are effectively reversed by CoSe/Ti_3C_2 and ERR-HJ treatment,

15214095, 0, Downloaded from https://advanced.onlinelibrary.wiley.com/doi/10.1002/adma.75394 by Sichuan University, Wiley Online Library on [23/10/2026]. See the Terms and Conditions (https://onlinelibrary.wiley.com/terms-and-conditions) on Wiley Online Library for rules of use; OA articles are governed by the applicable Creative Commons License

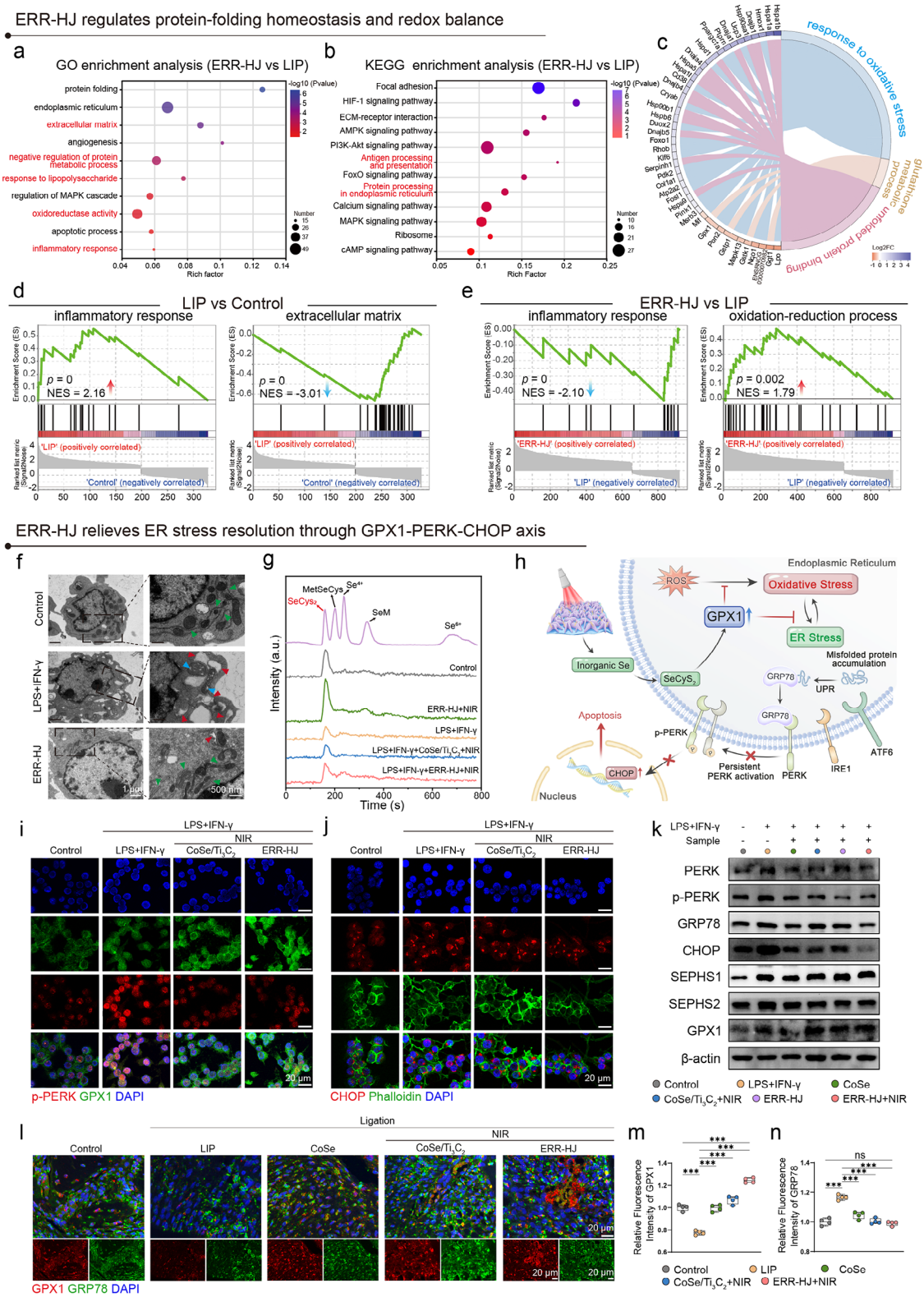


FIGURE 10 | Redox modulation and ER stress attenuation via GPX1-PERK-CHOP axis. (a,b) Transcriptomic changes in periodontal tissue under ERR-HJ-treated or untreated LIP periodontitis model (ERR-HJ vs. LIP), shown by GO and KEGG enrichment analyses of DEGs. (c) Chord diagram of enriched DEGs in the ERR-HJ-treated versus untreated LIP group, obtained by GO analysis. (d) GSEA showing enrichment of pathways in the LIP periodontitis model versus healthy Control, as well as (e) in the ERR-HJ-treated versus untreated LIP group. (f) TEM images of RAW 264.7 cells under different experimental conditions. Green triangles indicate normal ER lumen morphology; red triangles indicate dilated ER lumens; blue triangles indicate intramitochondrial vesicles. (g) Selenium metabolism in RAW 264.7 cells under different experimental conditions. (h) Schematic illustration of the mechanism by which the ERR-HJ alleviates ER stress through modulation of the GPX1-PERK-CHOP axis, created in BioRender. Chen, W. (2026) https://BioRender.com/5mlo8qx. (i) Immunofluorescence staining of GPX1 and p-PERK ($n = 4$ independent replicates). (j) Immunofluorescence images

15214095, 0, Downloaded from https://advanced.onlinelibrary.wiley.com/doi/10.1002/adma.75394 by Sichuan University, Wiley Online Library on [23/10/2026]. See the Terms and Conditions (https://onlinelibrary.wiley.com/terms-and-conditions) on Wiley Online Library for rules of use; OA articles are governed by the applicable Creative Commons License

especially ERR-HJ treatment under NIR (Figure 10l). Semiquantitative analysis of immunofluorescence further validates this trend (Figure 10m,n). A schematic illustration depicting the ERR-HJ-induced restoration of redox homeostasis and alleviation of ER stress via GPX1 upregulation-mediated attenuation dampening of the PERK-CHOP pathway is shown in Figure 10h. Given that both bacterial stimulation and excessive ROS can promote pro-inflammatory macrophage activation, the macrophage phenotypic changes following ERR-HJ treatment may not be attributed solely to ER stress alleviation, but also to reduced bacterial burden and redox restoration.

3 | Conclusion

In this work, we present the de novo design of an ER-regulating selenium-incorporated heterojunction that integrates interfacial electron transfer with host-directed stress regulation for the treatment of infection-associated inflammatory diseases. Formation of the CoSe/Ti_3C_2 heterointerface reconstructs the electronic structure and facilitates directional electron transport across the interface, enabling efficient utilization of oxidative microenvironment-derived electrons. Rather than simply scavenging ROS or generating additional radicals for disinfection, the heterojunction redirects electrons extracted from H_2O_2 toward bacterial membranes, resulting in electron accumulation, respiratory-chain disruption, and impaired bacterial bioenergetics. This mechanism transforms pathological oxidative cues into an active antibacterial process and provides an alternative paradigm to conventional ROS-centered antimicrobial strategies. Beyond antibacterial activity, the involvement of selenium metabolism endows the heterojunction with the ability to regulate intracellular stress responses. Through activation of GPX1-centered selenoprotein metabolism, ERR-HJ restores redox homeostasis and suppresses PERK-CHOP signaling, thereby interrupting the self-amplifying ER stress-oxidative stress-inflammation cycle that underlies tissue destruction in periodontitis. These coordinated effects ultimately restore osteoimmune homeostasis while directly enhancing the osteogenic differentiation of hPDLCs, collectively promoting periodontal regeneration. We propose that integrating interfacial electron engineering with endogenous stress regulation offers an enlightening conceptual framework for designing multifunctional biocatalytic heterojunctions for a broader range of bacterial infection-associated diseases.

4 | Experimental Section

Materials and methods, including synthesis and characterization of the CoSe/Ti_3C_2 heterojunction and ERR-HJ; SEM, TEM, AFM, DLS, SAED, elemental mapping, Raman, XPS, photophysical characterization, and finite-element simulation; DFT calculations, electronic structure analyses, charge redistribution, and catalytic mechanisms; ROS/RNS scavenging activity and catalytic kinetics; antibacterial and antibiofilm evaluations, bacterial transcriptomics, and metabolic analyses; cytocompatibility and osteogenic differentiation of hPDLCs; macrophage polarization, selenium metabolism, ER stress regulation, and osteoclastogenesis in RAW 264.7 cells; flow cytometry, RT-qPCR, immunofluorescence staining, and transmission electron microscopy; micro-CT, histological and immunohistochemical analyses, tissue transcriptomics, and biosafety evaluation of rats, are listed in the Supporting Information.

Author Contributions

Wanxi Chen: methodology, investigation, validation, data curation, conceptualization, formal analysis, writing – original draft, writing – review and editing, visualization. **Wenxuan He**: conceptualization, investigation, validation, formal analysis, methodology, data curation, writing – original draft, writing – review and editing, visualization. **Wenyu Dai**: methodology, funding acquisition. **Bin Li**: methodology, investigation. **Fan Yang**: data curation, funding acquisition. **Tian Chen**: validation, data curation. **Rui Shu**: funding acquisition, validation. **Ding Bai**: funding acquisition, supervision. **Yi Deng**: funding acquisition, writing – review and editing, supervision, conceptualization, project administration. **Hui Xu**: conceptualization, funding acquisition, writing – review and editing, supervision, project administration.

Acknowledgements

We thank Jing Zhou (Analytical & Testing Center, SCU) for assistance with CLSM and Qiang Guo (State Key Laboratory of Oral Diseases, West China Hospital of Stomatology, SCU) for assistance with micro-CT. We also would like to thank Yanping Huang from Center of Engineering Experimental Teaching for the help of SEM measurement. We thank Shanghai DaiSuan Technology (www.daisuan.com) for the help in DFT simulations. We would like to thank Dong Yu with Digital scanning system (WISLEAP WS-10), Linzhu Li with Digital scanning system (Olympus VS200) and Leica DMi 8 fluorescence microscope in Life Science Core Facilities (College of Life Sciences). The authors extend their gratitude to Scientific Compass (www.shiyanjia.com) for providing invaluable assistance. The authors would like to thank Ceshigo Research Service (www.ceshigo.com) for providing ESR testing. Thanks to eceshi (www.eceshi.com) for PL analysis. Part of the figures were created with BioRender.com.

Funding

This work is jointly funded by the National Key R&D Program of China (2024YFC2510700), the National Natural Science Foundation of China (32571536, 82271018, 32501345, 82571136, 82371002), the Sichuan Provincial International Science and Technology Innovation Cooperation Project (2026YFHZ0080), the Natural Science Foundation of Sichuan Province (2025ZNSFSC1590, 2024NSFSC0540), the China Postdoctoral Science Foundation (GZB20240483), as well as Research and Development Program, and the West China Hospital of Stomatology, Sichuan University (RD-02-202513).

of CHOP and FITC-phalloidin ($n = 4$ independent replicates). (k) Western blot analysis of PERK-CHOP pathway activation (PERK, p-PERK, GRP78 and CHOP) and selenoprotein (SEPHS1, SEPHS2 and GPX1) expression ($n = 3$ independent replicates). (l) Immunofluorescence images of GPX1 and GRP78 staining in the periodontal ligament ($n = 4$ independent replicates). (m,n) Semiquantification of relative fluorescence intensity of GPX1 and GRP78 in (l). All data are presented as mean ± SE. One-way ANOVA followed by Tukey's post hoc test was used. Significant differences between groups were indicated as $^{***}p < 0.001$, $^{**}p < 0.01$, $^{*}p < 0.05$, and ns represents not significant.

15214095, 0, Downloaded from https://advanced.onlinelibrary.wiley.com/doi/10.1002/adma.75394 by Sichuan University, Wiley Online Library on [23/10/2026]. See the Terms and Conditions (https://onlinelibrary.wiley.com/terms-and-conditions) on Wiley Online Library for rules of use; OA articles are governed by the applicable Creative Commons License

Conflicts of Interest

The authors declare no conflicts of interest.

Data Availability Statement

The data that support the findings of this study are available from the corresponding author upon reasonable request.

Supporting Information

References

1. G. Hajishengallis, "Periodontitis: From Microbial Immune Subversion to Systemic Inflammation," *Nature Reviews Immunology* 15, no. 1 (2015): 30–44, https://doi.org/10.1038/nri3785.

2. N. J. Kassebaum, E. Bernabé, M. Dahiya, B. Bhandari, C. J. Murray, and W. Marcenes, "Global Burden of Severe Periodontitis in 1990-2010," *Journal of Dental Research* 93, no. 11 (2014): 1045–1053, https://doi.org/10.1177/0022034514552491.

3. E. Bernabe, W. Marcenes, R. S. Abdulkader, et al., "Trends in the Global, Regional, and National Burden of Oral Conditions from 1990 to 2021: A Systematic Analysis for the Global Burden of Disease Study 2021," *The Lancet* 405, no. 10482 (2025): 897–910, https://doi.org/10.1016/S0140-6736(24)02811-3.

4. M. Pattamatta, I. Chapple, and S. Listl, "The Value-for Money of Preventing and Managing Periodontitis: Opportunities and Challenges," *Periodontology 2000* 98, no. 1 (2025): 56–64, https://doi.org/10.1111/prd.12569.

5. H. Petsos, B. Schacher, T. Ramich, et al., "Retrospectively Analysed Tooth Loss in Periodontally Compromised Patients: Long-Term Results 10 Years After Active Periodontal Therapy—Patient-Related Outcomes," *Journal of Periodontal Research* 55, no. 6 (2020): 946–958, https://doi.org/10.1111/jre.12786.

6. L. J. Suárez, R. M. Arce, C. P. Furquim, et al., "Antibiotic-Mediated Immune Modulation in Periodontitis," *Periodontology 2000* (2025): 1–28, https://doi.org/10.1111/prd.70011.

7. X. Chen, C. Shi, M. He, S. Xiong, and X. Xia, "Endoplasmic Reticulum Stress: Molecular Mechanism and Therapeutic Targets," *Signal Transduction and Targeted Therapy* 8, no. 1 (2023): 352, https://doi.org/10.1038/s41392-023-01570-w.

8. M. Jiang, Z. Li, and G. Zhu, "The Role of Endoplasmic Reticulum Stress in the Pathophysiology of Periodontal Disease," *Journal of Periodontal Research* 57, no. 5 (2022): 915–932, https://doi.org/10.1111/jre.13031.

9. M. Wang and R. J. Kaufman, "Protein Misfolding in the Endoplasmic Reticulum as a Conduit to Human Disease," *Nature* 529, no. 7586 (2016): 326–335, https://doi.org/10.1038/nature17041.

10. H. Domon, N. Takahashi, T. Honda, et al., "Up-regulation of the Endoplasmic Reticulum Stress-Response in Periodontal Disease," *Clinica Chimica Acta* 401, no. 1–2 (2009): 134–140, https://doi.org/10.1016/j.cca.2008.12.007.

11. K. Chaumonnot, S. Masson, H. Sikner, et al., "The HSP GRP94 Interacts with Macrophage Intracellular Complement C3 and Impacts M2 Profile during ER Stress," *Cell Death & Disease* 12, no. 1 (2021): 114, https://doi.org/10.1038/s41419-020-03288-x.

12. Y. Fu, H. Kim, D. S. Lee, et al., "Structural Insight Into TLR4/MD-2 Activation by Synthetic LPS Mimetics With Distinct Binding Modes," *Nature Communications* 16, no. 1 (2025): 4164, https://doi.org/10.1038/s41467-025-59550-3.

13. K. R. Bhattarai, T. A. Riaz, H. R. Kim, and H. J. Chae, "The Aftermath of the Interplay Between the Endoplasmic Reticulum Stress Response and Redox Signaling," *Experimental & Molecular Medicine* 53, no. 2 (2021): 151–167, https://doi.org/10.1038/s12276-021-00560-8.

14. J. Guo, R. Ren, K. Sun, et al., "PERK Controls Bone Homeostasis Through the Regulation of Osteoclast Differentiation and Function," *Cell Death & Disease* 11, no. 10 (2020): 847, https://doi.org/10.1038/s41419-020-03046-z.

15. P. Xue, B. Li, Y. An, et al., "Decreased MORF Leads to Prolonged Endoplasmic Reticulum Stress in Periodontitis-Associated Chronic Inflammation," *Cell Death & Differentiation* 23, no. 11 (2016): 1862–1872, https://doi.org/10.1038/cdd.2016.74.

16. J. Tan, H. Zhang, Y. Liu, et al., "Interfering With Proton and Electron Transfer Enables Antibacterial Starvation Therapy," *Science Advances* 11, no. 12 (2025): adt3159, https://doi.org/10.1126/sciadv.adt3159.

17. S. Wang, L. Wang, Y. Liu, et al., "Respiration Electron of Pathogenic Bacteria Activated ZnO@Viologen-COF Heterojunction to Boost Piezo-Phototronic Effect for Microbiota Regulation," *Science Bulletin* 70, no. 21 (2025): 3600–3613, https://doi.org/10.1016/j.scib.2025.09.019.

18. Q. Wu, T. Deng, J. Cheng, et al., "Constructing Interfacial Charge Transfer Channels and Electric Field in Violet Phosphorus-Based van der waals Heterojunction for Phototherapy of Periodontitis," *ACS Nano* 18, no. 18 (2024): 11988–12009, https://doi.org/10.1021/acsnano.4c02433.

19. B. Li, W. Yang, R. Shu, et al., "Antibacterial and Angiogenic (2A) Bio-Heterojunctions Facilitate Infectious Ischemic Wound Regeneration via an Endogenous–Exogenous Bistimulatory Strategy," *Advanced Materials* 36, no. 6 (2024): 2307613, https://doi.org/10.1002/adma.202307613.

20. X. Zhou, P. Wang, L. Xie, et al., "Molybdoenzymes-Emulating Bio-Heterojunction Hydrogel With Rapid Disinfection and Macrophage Reprogramming for Wound Regeneration," *Biomaterials* 320 (2025): 123284, https://doi.org/10.1016/j.biomaterials.2025.123284.

21. Z. He, X. Shao, X. Feng, et al., "Photothermal Sensitive Nano Heterojunction Triggering Ferroptosis and PANoptosis for Improving Tumor Immunotherapy," *Advanced Materials* 38, no. 37 (2026): 73503, https://doi.org/10.1002/adma.73503.

22. D. Wang, G. Qiu, H. Wang, et al., "Dual-Heterojunctions With Reversibly Photoactivated Structure Shift Alternately Decode Photocatalytic H_2 Burst and Cascade Catalytic ROS Birth to Repress Cancer," *Advanced Materials* 38, no. 4 (2026): 16305, https://doi.org/10.1002/adma.202516305.

23. Q. Liu, Y. Wang, J. Huang, et al., "Interfacial Engineering Enhancing Electron Transfer of CaF_2 Nanoparticles for Periodontitis Treatment of Sonotherapy and Bone Resorption," *ACS Nano* 19, no. 13 (2025): 13341–13355, https://doi.org/10.1021/acsnano.5c01112.

24. M. Qi, Q. Ding, Y. Shi, et al., "NIR-activated Nanodisguisers for Targeted Bactericidal Action and Enhanced Electron Transfer in Periodontitis Treatment," *Biomaterials* 324 (2026): 123487, https://doi.org/10.1016/j.biomaterials.2025.123487.

25. C. Ye, J. Liu, J. Ran, et al., "Polyphenol Mediated Zinc-Oxygen Synergistic Hydrogel Remodels Senescent Microenvironment for Periodontal Tissue Regeneration," *Nature Communications* 17, no. 1 (2026): 3719, https://doi.org/10.1038/s41467-026-70176-x.

26. K. Zheng, R. Song, R. Li, et al., "Nanomaterials for Refining Tumor Microenvironment and Enhancing Therapy in Head and Neck Squamous Cell Carcinoma: A Review," *Oncology and Translational Medicine* 10, no. 4 (2024): 151–161, https://doi.org/10.1097/ot9.0000000000000046.

27. D. Kang, J. Lee, J. Jung, et al., "Selenophosphate Synthetase 1 Deficiency Exacerbates Osteoarthritis by Dysregulating Redox Homeostasis," *Nature Communications* 13, no. 1 (2022): 779, https://doi.org/10.1038/s41467-022-28385-7.

28. H. Lai, L. Xu, C. Liu, et al., "Universal Selenium Nanoadjuvant With Immunopotentiating and Redox-Shaping Activities Inducing High-Quality Immunity for SARS-CoV-2 Vaccine," *Signal Transduction and Targeted Therapy* 8, no. 1 (2023): 88, https://doi.org/10.1038/s41392-023-01371-1.

29. E. Varone, D. Pozzer, S. Di Modica, et al., "SELENON (SEPN1) Protects Skeletal Muscle From Saturated Fatty Acid-Induced ER Stress and Insulin Resistance," *Redox Biology* 24 (2019): 101176, https://doi.org/10.1016/j.redox.2019.101176.

15214095, 0, Downloaded from https://advanced.onlinelibrary.wiley.com/doi/10.1002/adma.75394 by Sichuan University, Wiley Online Library on [23/10/2026]. See the Terms and Conditions (https://onlinelibrary.wiley.com/terms-and-conditions) on Wiley Online Library for rules of use; OA articles are governed by the applicable Creative Commons License

30. F. Yang, R. Shu, W. Dai, et al., "H_2Se-Evolving Bio-Heterojunctions Promote Cutaneous Regeneration in Infected Wounds by Inhibiting Excessive Cellular Senescence," *Biomaterials* 311 (2024): 122659, https://doi.org/10.1016/j.biomaterials.2024.122659.

31. M. Lele, S. Kapur, S. Hargett, N. M. Sureshbabu, and A. K. Gaharwar, "Global Trends in Clinical Trials Involving Engineered Biomaterials," *Science Advances* 10, no. 29 (2024): abq0997, https://doi.org/10.1126/sciadv.abq0997.

32. Y. Deng, Y. Gao, T. Li, et al., "Amorphizing Metal Selenides-Based ROS Biocatalysts at Surface Nanolayer Toward Ultrafast Inflammatory Diabetic Wound Healing," *ACS Nano* 17, no. 3 (2023): 2943–2957, https://doi.org/10.1021/acsnano.2c11448.

33. S. Cui, X. Zhong, Z. Li, et al., "Nanosecond Laser Synthesis of MXene-Derived TiO_2/High-Entropy Alloys for Photo-Assisted Zinc–Air Batteries," *Advanced Materials* 37, no. 35 (2025): 2504099, https://doi.org/10.1002/adma.202504099.

34. S. Wan, Y. Chen, C. Huang, et al., "Scalable Ultrastrong MXene Films With Superior Osteogenesis," *Nature* 634, no. 8036 (2024): 1103–1110, https://doi.org/10.1038/s41586-024-08067-8.

35. G. Du, Z. Liu, Z. Yu, et al., "Taurine Represses Age-Associated Gut Hyperplasia in Drosophila via Counteracting Endoplasmic Reticulum Stress," *Aging Cell* 20, no. 3 (2021): 13319, https://doi.org/10.1111/acel.13319.

36. J. McGaunn and J. A. Baur, "Taurine Linked With Healthy Aging," *Science* 380, no. 6649 (2023): 1010–1011, https://doi.org/10.1126/science.adi3025.

37. P. J. Murray, J. E. Allen, S. K. Biswas, et al., "Macrophage Activation and Polarization: Nomenclature and Experimental Guidelines," *Immunity* 41, no. 1 (2014): 14–20, https://doi.org/10.1016/j.immuni.2014.06.008.

38. T. Xu, S. Tan, S. Li, et al., "Synergistic Densification in Hybrid Organic-Inorganic MXenes for Optimized Photothermal Conversion," *Advanced Functional Materials* 34, no. 29 (2024): 2400424, https://doi.org/10.1002/adfm.202400424.

39. O. L. Lam, C. McGrath, H. M. Bandara, L. S. Li, and L. P. Samaranayake, "Oral Health Promotion Interventions on Oral Reservoirs of staphylococcus aureus: A Systematic Review," *Oral Diseases* 18, no. 3 (2012): 244–254, https://doi.org/10.1111/j.1601-0825.2011.01874.x.

40. R. J. Lamont, H. Koo, and G. Hajishengallis, "The Oral Microbiota: Dynamic Communities and Host Interactions," *Nature Reviews Microbiology* 16, no. 12 (2018): 745–759, https://doi.org/10.1038/s41579-018-0089-x.

41. V. M. Worlitzer, A. Jose, I. Grinberg, et al., "Biophysical Aspects Underlying the Swarm to Biofilm Transition," *Science Advances* 8, no. 24 (2022): abn8152, https://doi.org/10.1126/sciadv.abn8152.

42. J. Li, X. Liu, L. Tan, et al., "Zinc-Doped Prussian Blue Enhances Photothermal Clearance of Staphylococcus aureus and Promotes Tissue Repair in Infected Wounds," *Nature Communications* 10, no. 1 (2019): 4490, https://doi.org/10.1038/s41467-019-12429-6.

43. W. Li, E. S. Thian, M. Wang, Z. Wang, and L. Ren, "Surface Design for Antibacterial Materials: From Fundamentals to Advanced Strategies," *Advanced Science* 8, no. 19 (2021): 2100368, https://doi.org/10.1002/advs.202100368.

44. V. R. I. Kaila and M. Wikström, "Architecture of Bacterial Respiratory Chains," *Nature Reviews Microbiology* 19, no. 5 (2021): 319–330, https://doi.org/10.1038/s41579-020-00486-4.

45. M. Śmiga and T. Olczak, "Exploring Heme and Iron Acquisition Strategies of Porphyromonas gingivalis— Current Facts and Hypotheses," *FEMS Microbiology Reviews* 49 (2025): fuaf019, https://doi.org/10.1093/femsre/fuaf019.

46. M. F. Moradali and M. E. Davey, "Metabolic Plasticity Enables Lifestyle Transitions of *Porphyromonas gingivalis*," *NPJ Biofilms and Microbiomes* 7, no. 1 (2021): 46, https://doi.org/10.1038/s41522-021-00217-4.

47. T. K. Nemoto and Y. O. Nemoto, "Dipeptidyl-Peptidases: Key Enzymes Producing Entry Forms of Extracellular Proteins in Asaccharolytic Periodontopathic Bacterium Porphyromonas gingivalis," *Molecular Oral Microbiology* 36, no. 2 (2021): 145–156, https://doi.org/10.1111/omi.12317.

48. N. Lane and W. Martin, "The Energetics of Genome Complexity," *Nature* 467, no. 7318 (2010): 929–934, https://doi.org/10.1038/nature09486.

49. M. Scott, C. W. Gunderson, E. M. Mateescu, Z. Zhang, and T. Hwa, "Interdependence of Cell Growth and Gene Expression: Origins and Consequences," *Science* 330, no. 6007 (2010): 1099–1102, https://doi.org/10.1126/science.1192588.

50. B. Zou, Z. Xiong, Y. Yu, S. Shi, X. Li, and T. Chen, "Rapid Selenoprotein Activation by Selenium Nanoparticles to Suppresses Osteoclastogenesis and Pathological Bone Loss," *Advanced Materials* 36, no. 27 (2024): 2401620, https://doi.org/10.1002/adma.202401620.

51. V. M. Labunskyy, D. L. Hatfield, and V. N. Gladyshev, "Selenoproteins: Molecular Pathways and Physiological Roles," *Physiological Reviews* 94, no. 3 (2014): 739–777, https://doi.org/10.1152/physrev.00039.2013.

52. A. Kapara, A. Vannini, and B. Peck, "A Micronutrient With Major Effects on Cancer Cell Viability," *Nature Metabolism* 2, no. 7 (2020): 564–565, https://doi.org/10.1038/s42255-020-0244-3.

53. Z. Xiong, G. Huang, J. R. Huang, Y. Liu, L. He, and T. Chen, "Organic-Inorganic Covalent Selenium Reversing Ischemic Reperfusion Injury," *Nature Communications* 16, no. 1 (2025): 8030, https://doi.org/10.1038/s41467-025-62986-2.

54. S. Bae, K. Kim, K. Kang, et al., "RANKL-responsive Epigenetic Mechanism Reprograms Macrophages into Bone-resorbing Osteoclasts," *Cellular & Molecular Immunology* 20, no. 1 (2023): 94–109, https://doi.org/10.1038/s41423-022-00959-x.

55. M. Tsukasaki and H. Takayanagi, "Osteoimmunology: Evolving Concepts in Bone–Immune Interactions in Health and Disease," *Nature Reviews Immunology* 19, no. 10 (2019): 626–642, https://doi.org/10.1038/s41577-019-0178-8.

56. K. H. Park-Min, "Mechanisms Involved in Normal and Pathological Osteoclastogenesis," *Cellular and Molecular Life Sciences* 75, no. 14 (2018): 2519–2528, https://doi.org/10.1007/s00018-018-2817-9.

57. M. Tan, Y. Yin, X. Ma, et al., "Glutathione System Enhancement for Cardiac Protection: Pharmacological Options Against Oxidative Stress and Ferroptosis," *Cell Death & Disease* 14, no. 2 (2023): 131, https://doi.org/10.1038/s41419-023-05645-y.

58. S. Chen, S. Li, and H. Wang, "Remodeling Tumor-Associated Macrophages in the Tumor Microenvironment," *Oncology and Translational Medicine* 10, no. 6 (2024): 281–285, https://doi.org/10.1097/ot9.0000000000000063.

59. H. Kim, K. Lee, J. M. Kim, et al., "Selenoprotein W Ensures Physiological Bone Remodeling by Preventing Hyperactivity of Osteoclasts," *Nature Communications* 12, no. 1 (2021): 2258, https://doi.org/10.1038/s41467-021-22565-7.

60. Y. Tian, Y. Li, J. Liu, et al., "Photothermal Therapy With Regulated Nrf2/NF-κB Signaling Pathway for Treating Bacteria-Induced Periodontitis," *Bioactive Materials* 9 (2022): 428–445, https://doi.org/10.1016/j.bioactmat.2021.07.033.

61. N. Xu, X. Zhang, T. Qi, et al., "Biomedical Applications and Prospects of Temperature-Orchestrated Photothermal Therapy," *MedComm – Biomaterials and Applications* 1, no. 2 (2022): 25, https://doi.org/10.1002/mba2.25.

62. E. Özdemir, E. Bozkurt, F. M. Yazar, and M. B. Bozan, "Can Delta Neutrophil Index Values Predict the Success of Periodontal Treatment in Patients With Periodontitis?," *Clinical Oral Investigations* 28, no. 1 (2024): 82, https://doi.org/10.1007/s00784-023-05478-1.

63. L. Qiao, L. Men, S. Yu, et al., "Hepatic Deficiency of Selenoprotein S Exacerbates Hepatic Steatosis and Insulin Resistance," *Cell Death & Disease* 13, no. 3 (2022): 275, https://doi.org/10.1038/s41419-022-04716-w.

15214095, 0, Downloaded from https://advanced.onlinelibrary.wiley.com/doi/10.1002/adma.75394 by Sichuan University, Wiley Online Library on [23/10/2026]. See the Terms and Conditions (https://onlinelibrary.wiley.com/terms-and-conditions) on Wiley Online Library for rules of use; OA articles are governed by the applicable Creative Commons License

64. X. Su, H. Chen, H. Xiang, et al., "Selenium Participates in the Formation of Kidney Stones by Alleviating Endoplasmic Reticulum Stress and Apoptosis of Renal Tubular Epithelial Cells," *Redox Report* 29, no. 1 (2024): 2416825, https://doi.org/10.1080/13510002.2024.2416825.

65. P. Li, L. Zhu, C. Song, et al., "Triple-Functional Probiotics With Intracellularly Synthesized Selenium Nanoparticles for Colitis Therapy by Regulating the Macrophage Phenotype and Modulating Gut Microbiota," *ACS Nano* 19, no. 14 (2025): 14213–14232, https://doi.org/10.1021/acsnano.5c00574.

66. F. Yang, Y. Liu, H. Ren, G. Zhou, X. Yuan, and X. Shi, "ER-stress Regulates Macrophage Polarization Through Pancreatic EIF-2alpha Kinase," *Cellular Immunology* 336 (2019): 40–47, https://doi.org/10.1016/j.cellimm.2018.12.008.

67. Y. Tan, F. Zhang, J. Cao, et al., "GPX1-Driven Selenium Nanoplatform Reprograms MAMs-Mediated Organelle Crosstalk to Reverse Inflammatory Adipose Expansion in Thyroid Eye Disease," *Theranostics* 15, no. 18 (2025): 9601–9622, https://doi.org/10.7150/thno.117582.

68. H. Wu, Q. Shui, X. Luan, et al., "Triglycerides Induce Endoplasmic Reticulum Lipid Bilayer Stress to Activate PERK and Enhance Antifungal Immunity," *Cell Reports* 45, no. 2 (2026): 116976, https://doi.org/10.1016/j.celrep.2026.116976.

Supporting Information

Additional supporting information can be found online in the Supporting Information section.

Supporting Information is available from the Wiley Online Library.

Supporting File: adma75394-sup-0001-SuppMat.docx.

15214095, 0, Downloaded from https://advanced.onlinelibrary.wiley.com/doi/10.1002/adma.75394 by Sichuan University, Wiley Online Library on [23/10/2026]. See the Terms and Conditions (https://onlinelibrary.wiley.com/terms-and-conditions) on Wiley Online Library for rules of use; OA articles are governed by the applicable Creative Commons License